

Defect physics in complex energy materials

Khang Hoang^{1,*} and M D Johannes²

¹Department of Physics, North Dakota State University, Fargo, North Dakota 58108, United States

²Center for Computational Materials Science, Naval Research Laboratory, Washington, D.C. 20375, United States

*Corresponding author. E-mail: khang.hoang@ndsu.edu

Abstract.

Understanding the physics of structurally and chemically complex transition-metal oxide and polyanionic materials such as those used for battery electrodes is challenging, even at the level of pristine compounds. Yet these materials are also prone to and their properties and performance are strongly affected or even determined by crystallographic point defects. In this review, we highlight recent advances in the study of defects and doping in such materials using first-principles calculations. The emphasis is on describing a theoretical and computational approach that has the ability to predict defect landscapes under various synthesis conditions, provide guidelines for defect characterization and defect-controlled synthesis, uncover the mechanisms for electronic and ionic conduction and electrochemical extraction and (re-)insertion, and provide an understanding of the effects of doping. Though applied to battery materials here, the approach is general and applicable to any materials in which the defect physics plays a role or drives the properties of interest. Thus, this work is intended as an in-depth review of defect physics in particular classes of materials, but also as a methodological template for the understanding and design of complex functional materials.

Keywords: polarons, defects, doping, complex transition-metal oxides, polyanionic compounds, electronic and ionic transport, delithiation mechanism

1	Introduction	2
2	Computational approach	3
3	Electronic structure <i>vis-à-vis</i> polaron formation	7
4	Defect energetics and tuning defect landscapes	11
4.1	Layered oxides	12
4.2	Olivine phosphates	16
4.3	Spinel-type oxides	18
5	Delithiation mechanism and extraction voltage	20

6	Electronic and ionic conduction mechanisms	22
6.1	Defect migration energy barrier	22
6.2	Conductivity and activation energy	24
6.3	Interpretation of conductivity data	25
7	Theory of doping in complex materials	28
7.1	Lattice site preference and defect structure	28
7.2	Manipulation of charged native defects	30
7.3	Modification of the delithiation mechanism	32
8	Conclusions and outlook	34
	Acknowledgement	35
	References	35

1. Introduction

Materials for energy storage and conversion applications such as lithium-ion and sodium-ion batteries [1–4], supercapacitors [5,6], and solid-oxide fuel cells [7–9] are often complex transition-metal oxides and polyanionic compounds. As with other transition-metal oxides, they possess a rich physics arising from a subtle interplay among charge, spin, and lattice degrees of freedom [10,11]. These complex materials are also known to be prone to and their properties are strongly affected by crystallographic point defects. In lithium-ion batteries, for example, the presence of some of these defects in the electrode materials can be vital or detrimental to the battery performance [12–17]. A detailed understanding of defect thermodynamics and kinetics, including the synthesis–(defect) structure–property relationship, is thus essential to explaining, predicting, and optimizing the materials’ properties, and ultimately to the design and discovery of new materials with better performance. Progress in this area would also provide a better understanding of defect physics in strongly correlated functional materials in general.

Over the past two decades, computational studies have been indispensable in the development of a fundamental understanding of the physics and chemistry of battery materials. First-principles calculations based on density-functional theory (DFT) [18,19] have produced important results for and physical insights into various aspects of the materials, including atomic and electronic structure, voltage, capacity and cycling stability, power and rate capability, and thermal stability and safety [20–22]. These studies focused not only on bulk properties but also on the migration of alkali ions (often in conjunction with lithium vacancies) and, in some cases, small hole polarons and the effects of particular defects (e.g., antisite pairs) on ionic diffusion [14,23–28]. Far fewer studies have addressed defect physics and chemistry in a comprehensive manner.

Prior to 2011, several extensive studies of defects and doping in battery electrode materials were reported [29–31]. They were based on the traditional Kröger-Vink,

defect-reaction approach [32] and interatomic-potential simulations. The first systematic studies based on first-principles defect calculations were carried out for LiFePO_4 in 2011 [17,33]. Results from this work helped reconcile conflicting experimental reports on defect formation in the material, predicted the conditions under which LiFePO_4 with the lowest concentration of the detrimental iron antisite defects can be obtained, uncovered the electronic and ionic conduction mechanisms, and provided an understanding of the effects of doping. More importantly, the work demonstrated how systematic first-principles defect calculations can provide a comprehensive understanding of complex battery materials. Since 2012, there have been reports of extensive first-principles defect studies of a number of different materials, from those for lithium-ion battery cathodes [34–46] and anodes [47–49] to lithium-air [50–52]. Specific computational methods used in these studies vary from DFT within the local-density (LDA) or generalized gradient (GGA) approximation [53,54] and the DFT+ U extension [55] to a hybrid DFT/Hartree-Fock approach [56].

This article reviews recent progress in the study of defects and doping in lithium-ion battery electrode materials, emphasizing the use of *defect physics as a theoretical framework for understanding and designing complex functional materials* in general. In this approach, state-of-the-art and systematic first-principles defect calculations can be regarded as well-controlled computational experiments carried out to probe complex materials at the electronic and atomic level. Section 2 will outline the computational approach for defect studies. The power of the theoretical and computational approach will be illustrated in sections 3–7 with select examples drawn mainly from our work on layered transition-metal oxides, olivine phosphates, and spinel-type oxides. Direct comparisons with experiments will also be emphasized, particularly regarding defect characterization, defect-controlled synthesis, and electronic and ionic conductivities. Finally, we will end this topical review with conclusions and outlook in section 8.

2. Computational approach

A study of defect physics in a solid necessarily begins with an investigation of the *host* compound which acts as a reference for defect calculations (Note that the host material does *not* have to be a perfect stoichiometric compound). This includes the calculation of the atomic and electronic structure, phase stability, and any other bulk properties that may be deemed necessary to understand the physics of the host material. In subsequent calculations, defects‡ are treated within supercell models, in which a defect is included in a periodically repeated finite volume of the host compound which itself contains many original unit cells. The total-energy electronic structure calculations are based on DFT, often using the DFT+ U extension [55] or a hybrid DFT/Hartree-Fock approach [56] since it is known that DFT within LDA/GGA [53,54] fails catastrophically

‡ We often use the word “defect” as a generic term, referring to not only native defects intrinsic to the materials but also impurities (extrinsic defects) and defect complexes. Impurities, not to be confused with “impurity phases,” can be intentionally added (i.e., dopants) or unintentionally present.

in localized electron systems and particularly for transition-metal oxides. The hybrid functional approach is usually the method of choice because it treats *all* orbitals in the material on equal footing, unlike DFT+ U where *a priori* knowledge of parameters like the “Hubbard U ” for each orbital in each element in each local chemical environment is necessary. There is ample evidence that the electronic structure of complex materials is better represented by hybrid functionals than by other DFT approaches [27, 57]. Unless otherwise noted, the work we present in this review employs a specific implementation known as the HSE06 screened hybrid functional [58] available in the VASP code [59].

The *formation energy* of a general defect X in charge state q (with respect to the host lattice) is defined as [60–63]

$$E^f(X^q) = E_{\text{tot}}(X^q) - E_{\text{tot}}(\text{host}) - \sum_i n_i \mu_i^* + q(E_v + \mu_e) + \Delta^q, \quad (1)$$

where $E_{\text{tot}}(X^q)$ and $E_{\text{tot}}(\text{host})$ are the total energies of a supercell containing the defect and the defect-free supercell, respectively. μ_i^* is the atomic chemical potential, accounting for the species i either added ($n_i > 0$) or removed ($n_i < 0$) from the supercell to form the defect and representing the chemical reservoir with which the species is exchanged. μ_e is the electronic chemical potential, i.e., the Fermi level, which is the energy of the reservoir for electron exchange. As a convention, the Fermi level is referenced to the valence-band maximum (VBM) of the host (E_v). The chemical potentials can be regarded as variables; however, they are not free parameters. In fact, μ_i^* is subject to thermodynamic constraints and can be used to represent experimental conditions, e.g., during preparation or use of the material; μ_e is determined by the charge neutrality condition that involves all positively and negatively charged defects and free electrons and holes, if present, in the material (and can then be compared with the Fermi-level position obtained in experiments; see, e.g., [64]). Finally, Δ^q is a correction term to align the electrostatic potentials of the defect-free and defect supercells and to account for finite-size effects on the total energies of charged defects [65].

In thermodynamic equilibrium, the formation energy of a defect directly determines the concentration [62]:

$$c = N_{\text{sites}} N_{\text{config}} \exp\left(\frac{-E^f}{k_B T}\right), \quad (2)$$

where N_{sites} is the number of high-symmetry sites in the lattice (per unit volume) on which the defect can be incorporated, N_{config} is the number of equivalent configurations (per site), and k_B is the Boltzmann constant. Clearly, at a given temperature, a defect that has a lower formation energy will occur with a higher concentration. Note that the energy in equation (2) is, in principle, a free energy. However, the entropy and volume terms are neglected because they are usually small in solid phases. Besides, there is often significant cancellation between those terms in the host and in the reservoir [62, 63].

Let us illustrate with a specific example, namely a lithium vacancy in charge state q in the battery material LiCoO_2 :

$$E^f(V_{\text{Li}}^q) = E_{\text{tot}}(V_{\text{Li}}^q) - E_{\text{tot}}(\text{host}) + \mu_{\text{Li}}^* + q(E_v + \mu_e) + \Delta^q. \quad (3)$$

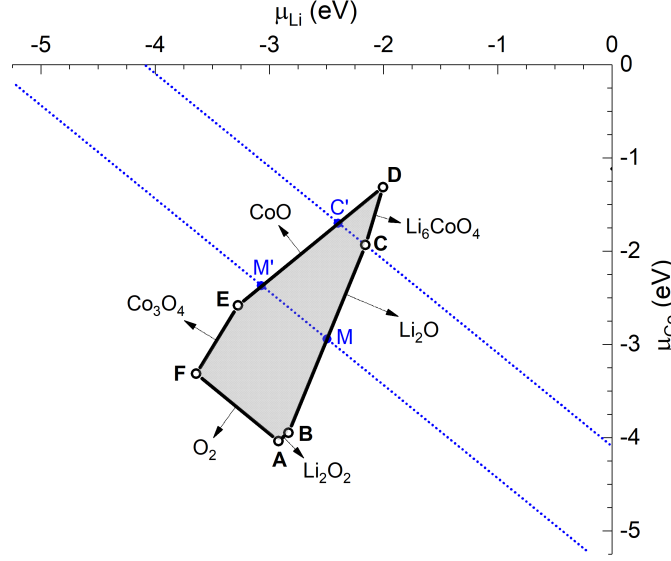


Figure 1. Chemical-potential phase diagram for LiCoO_2 . Only Li–Co–O phases that define the stability region of LiCoO_2 , shown as a shaded polygon, are indicated. The dotted (blue) lines correspond to the μ_{O} levels associated with oxygen in air at about 400°C (along MM') and 900°C (CC'). Produced with data from [36].

Here, $\mu_{\text{Li}}^* = E_{\text{tot}}(\text{Li}) + \mu_{\text{Li}}$, with $E_{\text{tot}}(\text{Li})$ being the total energy per atom of metallic Li. All the quantities in equation (3) can be obtained directly from the total-energy calculations, except μ_{Li} and μ_e . Although μ_{Li} cannot be calculated directly without making specific assumptions about the lithium reservoir, the upper and lower bounds on its values, as well as those for μ_{Co} and μ_{O} , can be determined by requiring that the host compound LiCoO_2 is stable against competing Li–Co–O phases [36]. Figure 1 shows the allowed range of the μ_{Li} and μ_{Co} values, bound in a polygon in the two-dimensional $(\mu_{\text{Li}}, \mu_{\text{Co}})$ space. For a given point in the polygon, the remaining μ_{O} variable is determined via the stability condition for the host [36]:

$$\mu_{\text{Li}} + \mu_{\text{Co}} + 2\mu_{\text{O}} = \Delta H(\text{LiCoO}_2), \quad (4)$$

where ΔH is the formation enthalpy calculated from DFT-based total energies. The determination of the Fermi level for a given set of μ_i values corresponding to a given point in the stability region will be made clear in section 4.1 when we discuss the energetics of all relevant defects in the material.

It should be noted that a phase diagram such as figure 1 is constructed based on zero-temperature energies. This, however, does not mean that temperature effects on the formation energy are all ignored. In fact, they can be included in the chemical potentials. For example, μ_{O} is related to temperature and pressure via the expression [66]

$$\mu_{\text{O}}(T, p) = \mu_{\text{O}}(T, p_{\circ}) + \frac{1}{2}k_{\text{B}}T \ln \frac{p}{p_{\circ}}, \quad (5)$$

where p and p_{\circ} are, respectively, the partial pressure and reference partial pressure of O_2 gas. The reference state of $\mu_{\text{O}}(T, p)$ can be chosen to be half of the total energy of

an isolated O_2 molecule at 0 K. In figure 1, $\mu_{\text{O}} = 0$ eV along the AF line, corresponding to the value at 0 K. More experimentally relevant values can be estimated by using the actual synthesis conditions which place even stronger bounds on the atomic chemical potentials. For example, LiCoO_2 is often synthesized at about 400–900°C in air [67]. This translates into a range of μ_{O} values from -0.74 eV (along the MM' line in figure 1) to -1.40 eV (the CC' line) with the upper and lower bounds obtained from the Gibbs free energy of O_2 gas at 0.21 atm and 400°C and 900°C, respectively [68]. The stability region enclosed by points M , C , C' , and M' in figure 1 can be considered as representing approximately the actual conditions under which LiCoO_2 is prepared. Here, as a first approximation, temperature-dependent effects are considered only for the gaseous (O_2) phase; the effects for the solid phases are ignored as they are often small [63].

In the methodology just described, native defects, including *charged* defects, and their energetics can thus be studied *individually* and the dependence of their formation energy and hence concentration on the Fermi level and the relative abundance of the host compound’s constituent elements in the synthesis environment can be explicitly examined. Effects of impurities, either intentionally added or unintentionally present in the material, can be examined in the same manner; see also section 7. It should be noted that, though first-principles defect calculations are often carried out using large supercell models and assuming the dilute defect limit, direct defect–defect interaction can be studied by explicitly considering defect complexes in the calculations. Also note that this approach for defect calculations is different from the traditional Kröger-Vink approach where calculations are carried out only for neutral defects or neutral defect complexes, e.g., Frenkel and Schottky pairs, based on pre-selected defect reactions [32]. Any specific defect reaction, if thermodynamically possible, is already included in the chemical-potential phase diagram and corresponds to a point in the stability region.

To understand defect physics in complex energy materials and its implications on the materials’ properties and performance, one needs to carry out systematic calculations for all possible electronic and ionic defects (polarons, vacancies, interstitials, and antisites) as well as impurities, if present. The calculations produce information about the atomic and electronic structure and energetics of each defect, and the *defect landscape* [17], which shows the relative formation energy (and hence concentration) of all defects, as a function of the atomic chemical potentials, i.e., synthesis conditions. Migration barriers of defects, especially those that can participate in charge and mass transport, can be computed using standard techniques such as the nudged elastic band method [69]. All this information from the calculations can then be employed to explore all possible defect landscapes, provide guidelines for defect characterization and defect-controlled synthesis, uncover the mechanisms for electronic and ionic conduction and electrochemical extraction and (re-)insertion, and understand the effects of doping.

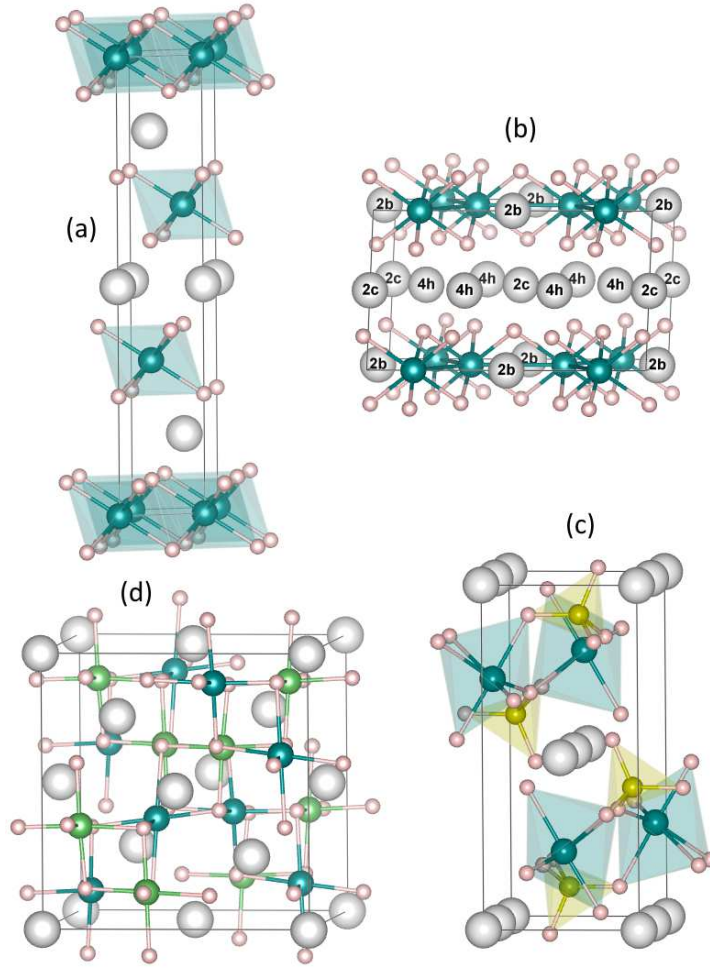


Figure 2. Atomic structure of (a) LiCoO_2 (trigonal, $R\bar{3}m$), (b) Li_2MnO_3 (monoclinic, $C2/m$), (c) LiFePO_4 (orthorhombic, $Pnma$), and (d) LiMn_2O_4 (slightly tetragonally distorted from cubic $Fd\bar{3}m$ [40]). Large (gray) spheres are Li, medium (blue or green) spheres are transition metals, small (yellow) spheres are P, and smallest (pink) spheres are O. The inequivalent Li Wyckoff positions in Li_2MnO_3 are indicated. In LiMn_2O_4 , the Mn^{3+} and Mn^{4+} ions are presented as dark (blue) and light (green) medium spheres. All the structures are visualized using the VESTA package [70].

3. Electronic structure *vis-à-vis* polaron formation

Before discussing defect physics in complex materials, let us first examine their atomic and electronic structure. Figure 2 shows the crystal structure of representatives from different classes of battery electrode materials: layered oxides, olivine phosphates, and spinel-type oxides. LiCoO_2 has alternate layers of Li^+ and $(\text{CoO}_2)^-$ in which cobalt is stable as low-spin Co^{3+} and locates at the center of octahedra formed by oxygen. In a simple ionic model, the material can be regarded as an ordered arrangement of Li^+ , Co^{3+} , and O^{2-} [36]. The structure of LiNiO_2 and LiMnO_2 is slightly distorted compared to that of LiCoO_2 , due to the strong Jahn-Teller effects associated with low-spin Ni^{3+} and high-spin Mn^{3+} ions [36, 41]. In layered mixed transition-metal oxides $\text{LiNi}_{1/3}\text{Co}_{1/3}\text{Mn}_{1/3}\text{O}_2$

($\text{NCM}_{1/3}$, also known as NMC333 or NMC111) and $\text{LiNi}_{1/3}\text{Co}_{1/3}\text{Al}_{1/3}\text{O}_2$ ($\text{NCA}_{1/3}$), not shown in the figure, the transition-metal layer contains a mixture of Ni^{2+} , low-spin Co^{3+} , and Mn^{4+} ($\text{NCM}_{1/3}$) or low-spin Ni^{3+} , low-spin Co^{3+} , and Al^{3+} ($\text{NCA}_{1/3}$) [44]. Li-rich Li_2MnO_3 , also known as $\text{Li}[\text{Li}_{1/3}\text{Mn}_{2/3}]\text{O}_2$, has a layered structure similar to that of LiMnO_2 but with one-third of the atoms in the Mn layer replaced by lithium; as a result, each oxygen in Li_2MnO_3 has only two Mn neighbors, instead of three as in LiMnO_2 . Manganese is stable as Mn^{4+} and the material can be regarded as consisting of Li^+ , Mn^{4+} , and O^{2-} [41]. In LiFePO_4 , lithium forms one-dimensional channels and the transition metal locates at the center of a slightly distorted FeO_6 octahedron. Iron is stable as high-spin Fe^{2+} and the compound can be regarded as consisting of Li^+ , Fe^{2+} , and $(\text{PO}_4)^{3-}$ [17]. Finally, LiMn_2O_4 is a mixed-valence compound containing both Jahn-Teller active (high-spin Mn^{3+}) and non-active (Mn^{4+}) ions. This spinel-type oxide is known to possess a cubic structure at room temperature but transforms into a partially charge-ordered orthorhombic or tetragonal phase at low temperatures [71–74]. The supercell model with the $\text{Mn}^{3+}/\text{Mn}^{4+}$ ordering shown in figure 2(d) was found to have the lowest total energy (at 0 K) among possible $\text{Mn}^{3+}/\text{Mn}^{4+}$ arrangements [40].

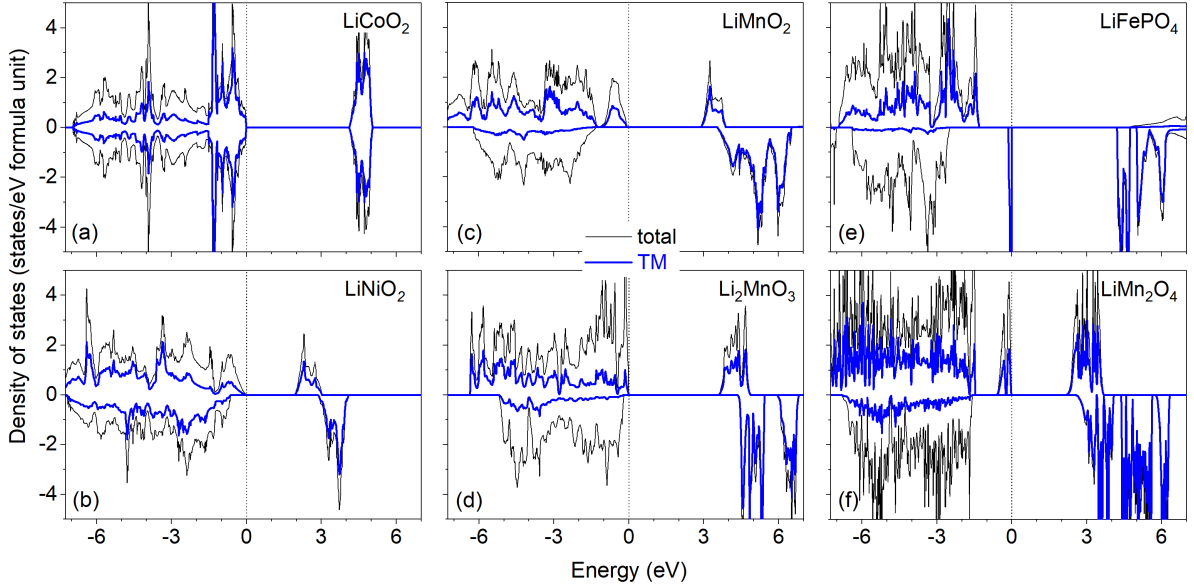


Figure 3. Total and partial densities of states of (a) LiCoO_2 , (b) LiNiO_2 , (c) LiMnO_2 , (d) Li_2MnO_3 , (e) LiFePO_4 , and (f) LiMn_2O_4 , obtained in HSE06 calculations. The ferromagnetic spin configuration was assumed for the transition-metal (TM) array in the lattice. The zero of the energy (at 0 eV) is set to the highest occupied state.

In the vast majority of battery electrode materials, including those explicitly discussed in this review, the transition-metal ion, often also the redox center, is octahedrally coordinated with oxygen. This gives rise to the well-known crystal-field splitting of the five transition-metal d -states into an upper strong anti-bonding doublet (e_g) manifold with significant oxygen admixture, and a lower weak- or non-bonding (t_{2g}) triplet manifold with minimal oxygen admixture. These electronic states form both

the valence and conduction bands and their dispersion and transition-metal vs. oxygen content have a strong effect on the type of defects that can form, as well as on other battery properties such as voltage [44,75], chemical stability [76], and transport efficiency [27]. The nature of these bands is determined by the electron count (charge state) of the transition metal and by a competition between crystal-field splitting and Hund's rule which determines whether the system is in a high-spin or low-spin configuration.

Figure 3 shows the electronic density of states (DOS) of the six compounds (including those shown in figure 2). Both the total DOS and the partial DOS (PDOS) of the transition metal are plotted, with the two spin channels plotted separately on the positive and negative y -axis. The difference between the total DOS and the transition-metal PDOS can be understood as the amount of oxygen character since the Li states are high up in the conduction band. It is instructive to first compare two of the most common battery materials: LiCoO_2 and LiFePO_4 . In the former, the Co ion is in the +3 charge state (d^6 configuration). The crystal field from the Co $3d$ and O $2p$ bonding is strong enough to overcome the Hund's coupling and produces a low-spin ground state ($t_{2g}^6 e_g^0$) with all electrons in the lower weakly anti-bonding t_{2g} complex. Due to the Co d -O p interaction, this complex is fairly dispersive (broad DOS); see figure 3(a). In LiFePO_4 , the Fe ion is in the +2 state (also d^6 configuration). But, because the PO_4 unit is already tightly bound, the bonding between Fe and O is weak and the crystal-field splitting is small; as a result, the ground-state configuration is high spin ($t_{2g}^4 e_g^2$). This leaves the highest energy electron in the minority spin anti-bonding t_{2g} complex, like LiCoO_2 , but with significantly less dispersion and oxygen admixture, giving rise to a sharply peaked Fe-dominant DOS just below the VBM; see figure 3(e).

As a general rule, the bonding between oxygen and transition metal increases as one moves right across the $3d$ row of the periodic table. Within a materials (structural) class, then, a rightward shift of the transition-metal ion increases the crystal-field splitting and the amount of oxygen in the valence band, and decreases the tendency toward hole localization. For instance, in LiCoO_2 , the Co character clearly dominates the DOS at the VBM. In LiNiO_2 , by contrast, the Ni character is less than 50% of the total [36], reflecting the greater oxygen admixture; see figure 3(b). LiMnO_2 here appears to violate this rule, showing rather strong oxygen character in the valence band despite being leftward of Co and Fe in the periodic table; see figure 3(c). This is, however, precisely *because* of the weaker bonding between Mn $3d$ and O $2p$ states that weakens the crystal-field splitting, resulting in a high-spin rather than low-spin ground state. Electrons at the top of the valence band are therefore in the comparatively oxygen-rich e_g states rather than the oxygen-poor t_{2g} . Regarding the other Mn-based compounds, the top of the valence band of LiMn_2O_4 is predominantly composed of the Mn $3d$ states, specifically from the Mn^{3+} ions [40], whereas that of Li_2MnO_3 is predominantly O $2p$ states [41]. The much higher oxygen content in the case of Li_2MnO_3 also comes from the fact that oxygen in this oxide is undercoordinated, compared to that in LiMnO_2 . For all compounds presented in figure 3, the conduction-band bottom is predominantly composed of the transition-metal $3d$ states. The conduction-band bottom of LiMn_2O_4 , in particular,

consists predominantly of the Mn 3d states from the Mn⁴⁺ ions [40]. For the electronic structure of mixed transition-metal oxides NCM_{1/3} and NCA_{1/3}, see, e.g., [44].

In the discussion above, we paid particular attention to the electronic states near the band edges. This is because they are relevant to transport and electrochemical processes. For example, in an oxidation reaction, electrons are removed from the material which results in electron holes being introduced at the VBM; a reduction reaction, on the other hand, involves addition of electrons to the material and these electrons then reside at the conduction-band minimum (CBM). The type of electronic defects that can form depends on whether the holes (electrons) can localize into polarons or delocalize into the valence (conduction) band. The *necessary condition* for a hole (electron) to localize on a particular transition metal is that the contribution of that transition metal to the electronic states at the VBM (CBM) of the host compound is larger than or equal to that from any other transition metal in the supercell and is larger than the contribution from any oxygen atom. Given that interplay between electronic structure and polaron formation, it becomes essential to reproduce correctly the electronic structure.

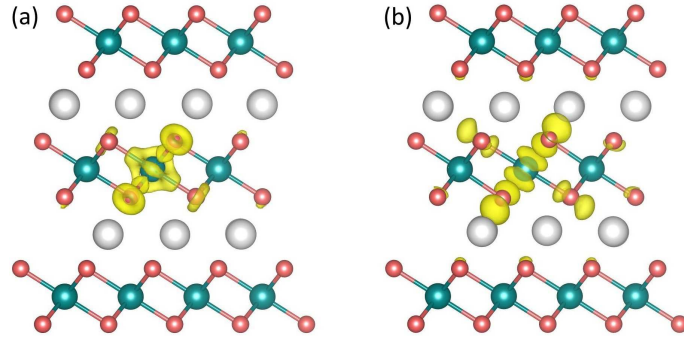


Figure 4. Charge densities associated with hole and electron polarons in LiCoO₂ [36]: (a) η^+ and (b) η^- , corresponding to Co⁴⁺ and Co²⁺ at a Co³⁺ lattice site. Large (gray) spheres are Li, medium (blue) spheres are Co, and smallest (red) spheres are O.

Figure 4 shows the local lattice environments and charge densities associated with hole (η^+) and electron (η^-) polarons§ in LiCoO₂ [36]. η^+ and η^- here are basically low-spin Co⁴⁺ and high-spin Co²⁺, respectively, at a Co³⁺ site in the host lattice. These electronic defects are called free or *unbound* polarons as they are stable even in the absence of other native defects or impurities; they are also called *small polarons* [77] as the local lattice distortion induced by the presence of the localized hole or electron is limited mainly to the neighboring O atoms [36]. Unbound small polarons were also reported to occur in LiNiO₂ [36], LiMnO₂ [41], NCM_{1/3}, NCA_{1/3} [44], LiFePO₄ [14, 17, 26], LiMn₂O₄ [40], consistent with the electronic structure discussed earlier, as well as in many other battery electrode materials. In Li-rich layered Li₂MnO₃, the addition of an electron also results in a small electron polaron (η^-), which is basically

§ In this review, a hole (electron) polaron formed on a transition-metal ion is referred commonly to as η^+ (η^-); their true identities should be evident in the context of a specific host compound. Also note that, in the literature, hole and electron polarons are sometimes denoted as p^+ and p^- , respectively.

high-spin Mn^{3+} at a Mn^{4+} site. The removal of an electron results in a delocalized hole being introduced at the VBM, consistent with the fact the VBM of Li_2MnO_3 is predominantly composed of the relatively delocalized O $2p$ states. More interestingly, it is also because of that feature in the electronic structure that *bound* hole polarons (η_{O}^+) at oxygen sites were found to form in the presence of other defects, e.g., negatively charged lithium vacancies (V_{Li}^-) [41]. This defect, first reported in [41], is essentially O^- (with a calculated magnetic moment of $0.69\mu_{\text{B}}$) at an O^{2-} site in the host lattice and can be referred to as “bound oxygen hole polaron” [41], “localized electron hole states on oxygen” [78, 79], or “ O^- bound polaron” [80]. The formation of η_{O}^+ provides a clear evidence for the anionic redox activity in Li_2MnO_3 and related materials; see sections 5 and 7.3 for further discussions of η_{O}^+ and its implications on the delithiation mechanism and electronic conduction.

In this section, we have thus showed how one can tell from the electronic structure of a material if and where a hole or electron polaron can form. Whether the polaron can actually occur in the material with a significant concentration, when thermally activated, depends on its formation energy. A hole (electron) polaron is a charged defect, i.e., its formation energy is dependent on the position of the Fermi level [see equation (1)]. The determination of the polaron formation energy would thus require information about the energetics of all other possible defects that may occur in the material; see section 4. Polarons can also be activated during oxidation and/or reduction processes [41]. Lithium extraction from a lithium-ion battery cathode during charging, for instance, often leads to simultaneous formation of hole polarons and negatively charged lithium vacancies in the electrode material; here, the more relevant quantity is the extraction voltage, instead of the defect formation energy; see section 5. The role of polarons as charge-carrying defects in (thermally activated) electronic conduction in complex materials will be discussed in section 6. The interplay between electronic structure and polaron formation (and hence presence of active redox centers) has also been shown to be essential to the understanding of materials for pseudocapacitors [81, 82] and solid-oxide fuel cells [64].

4. Defect energetics and tuning defect landscapes

In addition to the small hole and electron polarons discussed in section 3, other possible native defects include vacancies, interstitials, and antisites. Defects can be *thermally activated*, e.g., during materials preparation at high temperatures and get trapped inside the materials when cooling down to room temperature. Certain defects may thus be present with significant concentrations in the materials and affect their properties and performance. Here, we discuss structure and energetics of native defects and the dependence of defect landscapes on the synthesis conditions, based on recent work on layered oxide [36, 41, 44], olivine phosphate [17], and spinel-type oxide [40] materials.

4.1. Layered oxides

Defects are common in layered oxide materials. LiCoO_2 prepared at low temperatures, for example, exhibits significant Co/Li disorder and poor electrochemical performance [67]. Also, experimental studies of the magnetic properties always find the presence of localized magnetic moments in LiCoO_2 samples [83]. It has been reported that truly stoichiometric LiCoO_2 is possible; however, it requires rather delicate experimental procedures to prepare [84]. In fact, the commercially available LiCoO_2 is often made deliberately Li-overstoichiometric. An even more striking example is that of LiNiO_2 , for which the stoichiometric compound with all Ni^{3+} does not really exist. The long-range Jahn-Teller distortion and magnetic ordering (associated with low-spin Ni^{3+}) expected in defect-free LiNiO_2 is absent in real samples and the material always has a significant concentration of Ni ions at the Li site [85–90]. LiMnO_2 , on the other hand, is prepared via ion exchange from NaMnO_2 because the synthesis at high temperatures often results in an orthorhombic phase [91, 92]. The material is known to have strong cation mixing [91] and poor electrochemical performance which is usually ascribed to structural phase instabilities [93]. Manganese antisites have also been observed in Li-rich layered oxide Li_2MnO_3 , i.e., $\text{Li}[\text{Li}_{1/3}\text{Mn}_{2/3}]\text{O}_2$, under certain synthesis conditions [94].

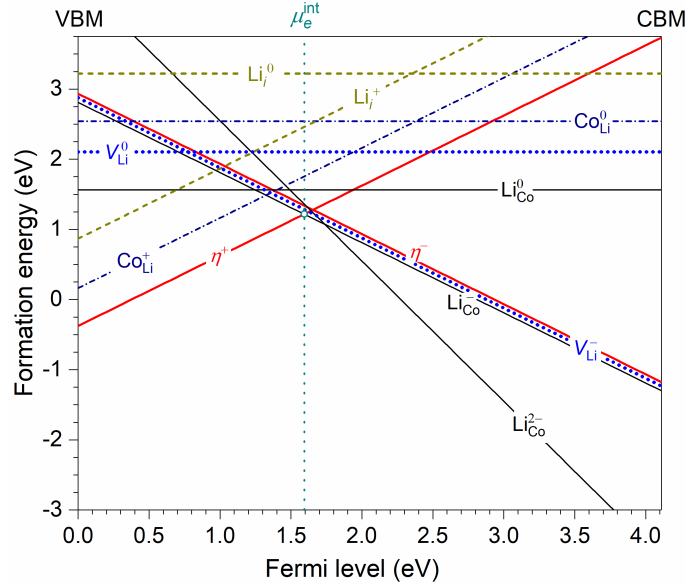


Figure 5. Formation energies of relevant native defects in LiCoO_2 , plotted as a function of the Fermi level. The energies are obtained at point M in the chemical-potential phase diagram (figure 1). The slope indicates the charge state [i.e., q in equation (1)]: positively (negatively) charged defects have positive (negative) slopes. μ_e^{int} is the position of the Fermi level determined by the charge neutrality condition involving the native/intrinsic defects. Produced with data from [36].

Figure 5 shows the formation energies of relevant defects in LiCoO_2 reported in [36]. These defects include unbound small hole (η^+ , i.e., low-spin Co^{4+}) and electron (η^- , i.e., high-spin Co^{2+}) polarons mentioned in section 3, lithium vacancies (V_{Li}) and interstitials

(Li_i), and lithium (Li_{Co}) and cobalt (Co_{Li}) antisites; other defects are not included because they have much higher energies (at least in the bulk; more discussion later). Each defect type may have several charge states, corresponding to different values for q in equation (1). However, among the ionic defects included in figure 5, only the following defect configurations are the true charge states: V_{Li}^- (i.e., a void formed by the removal of a Li^+), Li_i^+ (additional Li^+ ion at an interstitial site), $\text{Li}_{\text{Co}}^{2-}$ (Li^+ replacing Co^{3+} at a Co site), and Co_{Li}^+ (high-spin Co^{2+} replacing Li^+ at a Li site). These configurations are regarded as *elementary* defects. Other charge states are, in fact, defect complexes consisting of the elementary ionic defects and polaron(s). For example, the neutral charge state of V_{Li} , nominally denoted as V_{Li}^0 , is a complex of V_{Li}^- and η^+ ; similarly, Co_{Li}^0 is a complex of Co_{Li}^+ and η^- , and Li_{Co}^0 is a complex of $\text{Li}_{\text{Co}}^{2-}$ and two η^+ [36].

In the absence of electrically active impurities or when they occur with lower concentrations than the charged native defects, the Fermi level of LiCoO_2 is at $\mu_e = \mu_e^{\text{int}}$ (“int” stands for “intrinsic”) where charge neutrality is maintained, i.e., positive and negative charges originating from the native defects are balanced. Because of the strong (exponential) dependence of the concentration on the formation energy, μ_e^{int} is essentially “pinned” at the position where the lowest-energy positively and negatively charged defects have equal formation energies. In the example presented in figure 5, μ_e^{int} is predominantly determined by η^+ and $\text{Li}_{\text{Co}}^{2-}$. The energetically most stable configurations of the vacancies, interstitials, and antisites at μ_e^{int} are V_{Li}^- , Li_i^+ , $\text{Li}_{\text{Co}}^{2-}$ (a complex of $\text{Li}_{\text{Co}}^{2-}$ and η^+), and Co_{Li}^+ . Cobalt is thus most stable as high-spin Co^{2+} at the Li site, as opposed to being low-spin Co^{3+} at its original (Co) lattice site. It is noted that μ_e^{int} is far from both the band edges; as a result, band-like carriers would be negligible. In fact, the Fermi level of the system cannot come close to the VBM or CBM, otherwise the formation energy of certain charged native defects will become very small or even negative, see figure 5, and the host compound will become unstable. This has important implications for the electronic conduction and doping mechanisms as discussed in sections 6 and 7.

The defect landscape shown in figure 5 is not the only scenario that may occur. In fact, as reported in [36], defect energetics is sensitive to the choice of the atomic chemical potentials and hence the synthesis conditions. Under the conditions at point M' in figure 1, for example, the lowest-energy native defects in LiCoO_2 are Co_{Li}^+ and V_{Li}^- , whereas at points C and C' they are Co_{Li}^+ and η^- ; for more results at other points in the chemical-potential phase diagram, see [36]. The scenario reported by Gummow *et al.* [67], where significant Co/Li disorder was observed experimentally, could be identified with that obtained under the conditions somewhere between M and M' in the chemical-potential diagram. The experimental preparation of Li-overstoichiometric LiCoO_2 is likely carried out under the conditions somewhere near M and between points M and C where the host is in equilibrium with Li_2O as the impurity phase is often observed when preparing LiCoO_2 in Li-excess (Co-deficient) environments [84, 95]. From the defect landscape in figure 5, the chemical formula for the Li-overstoichiometric samples can be written as $\text{Li}_{1+\delta}\text{Co}_{1-\delta}\text{O}_2$ or, more explicitly, as $\text{Li}[\text{Co}_{1-3\delta}^{3+}\text{Li}_{\delta}^+\text{Co}_{2\delta}^{4+}]\text{O}_2$ where each $\text{Li}_{\text{Co}}^{2-}$ is charge compensated by two η^+ , assuming that other defects have negligible concentrations.

The excess Li thus goes into the Co site, instead of an interstitial site. This is because Li interstitials are energetically less favorable in LiCoO_2 [36], as also seen in figure 5. The results reviewed here thus indicate that *one can tune the defect landscape in the material by tuning the synthesis conditions*. Note that, as the defect landscape changes, the Fermi-level position μ_e^{int} changes accordingly [36]. Also, in all defect landscapes, the lowest-energy native defects in the material always contain low-spin Co^{4+} (in the form of the η^+ defect) and/or high-spin Co^{2+} (in the form of η^- or Co_{Li}^+) [36]. This is consistent with the presence of localized magnetic moments observed in experiments [83].

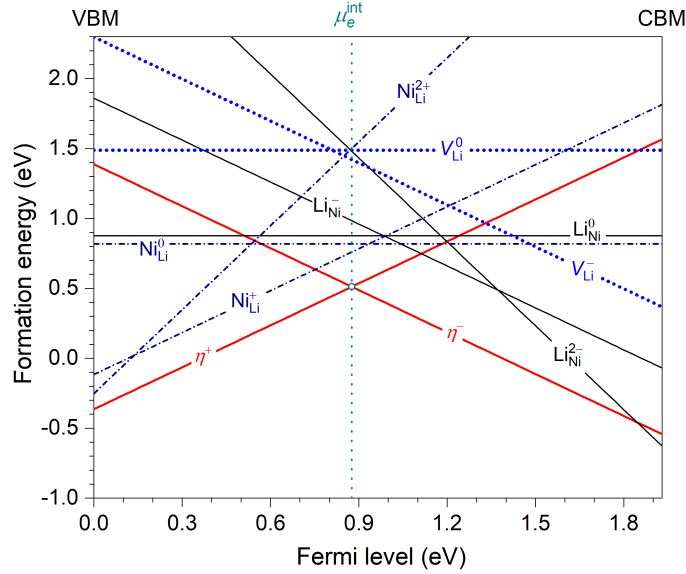


Figure 6. Formation energies of relevant native defects in LiNiO_2 . The energies are obtained at a point in the chemical-potential phase diagram where LiNiO_2 is in equilibrium with Li_2O and Li_2NiO_2 . Produced with data from [36].

Defect landscapes in different materials are often very different. Figure 6 shows a representative landscape in LiNiO_2 . As reported in [36], unbound small polarons η^+ (i.e., low-spin Ni^{4+}) and η^- (i.e., Ni^{2+}) are always the lowest-energy native defects, independent of the atomic chemical potentials. These polarons “pin” the Fermi level of LiNiO_2 at μ_e^{int} , where charge neutrality is maintained, and have a formation energy of only 0.51 eV. η^+ and η^- in LiNiO_2 can be activated via an *electron-hole polaron pair* mechanism (somewhat similar to the Frenkel pair mechanism for ionic defects [96]); here, one electron is transferred from one Ni^{3+} to another which results in the formation of Ni^{4+} and Ni^{2+} , i.e., the $\eta^+-\eta^-$ pair. Our explicit calculations for this polaron pair, in which the two Ni sites are nearest neighbors, show that it has a formation energy of 0.46 eV. With such a low energy, η^+ and η^- are easy to form, i.e., a certain amount of Ni^{3+} ions, estimated to be about 8% when the material is prepared at 800°C, undergo *charge disproportionation*: $2\text{Ni}^{3+} \rightarrow \text{Ni}^{4+} + \text{Ni}^{2+}$. Note that in the concentration estimation, $N_{\text{config}} = 6$ for the $\eta^+-\eta^-$ pair and thermodynamic equilibrium is assumed. The nickel antisite Ni_{Li}^+ (i.e., Ni^{2+} at a Li site) also has a low formation energy [36]. These results explain the experimental observations mentioned earlier, including the difficulty

in synthesizing LiNiO_2 with all Ni^{3+} at high temperatures, the absence of long-range Jahn-Teller distortion and magnetic ordering, and the presence of nickel antisites [85–90]. Note that, although the formation energy of $\eta^+-\eta^-$ (as well as that of η^+ and η^- at μ_e^{int}) is independent of the atomic chemical potentials, i.e., one cannot eliminate the charge disproportionation by simply tuning the synthesis conditions [36], the concentration of Ni^{4+} and Ni^{2+} may be reduced by lowering the synthesis temperature, see equation (2), assuming that the system is still in (or close to) thermodynamic equilibrium.

Regarding the Mn-based layered oxides, the lowest-energy positively and negatively charged native defects in LiMnO_2 can be the small hole polaron η^+ (i.e., Mn^{4+}) and V_{Li}^- , η^+ and $\text{Li}_{\text{Mn}}^{2-}$, Mn_{Li}^+ and $\text{Li}_{\text{Mn}}^{2-}$, or Mn_{Li}^+ and V_{Li}^- , depending on the chosen set of the atomic chemical potentials. Under all possible synthesis conditions, the defect landscape of the material is characterized by the presence of low-formation-energy antisites Mn_{Li}^+ and $\text{Li}_{\text{Mn}}^{2-}$ [41]. These findings are thus consistent with experiments showing strong cation mixing in LiMnO_2 [91, 92]. As discussed in [41], the antisites can act as nucleation sites for the formation of orthorhombic LiMnO_2 during synthesis or spinel LiMn_2O_4 during electrochemical cycling, which leads to inferior cycling stability [93]. In Li_2MnO_3 , Mn_{Li}^+ (i.e., high-spin Mn^{2+} at the Li site, $4h$ or $2c$) was also found to have a low formation energy under Li-deficient and/or reducing conditions [41], which is consistent with the presence of these antisites in the “oxygen-deficient $\text{Li}_2\text{MnO}_{3-x}$ ” samples synthesized in the presence of strong oxygen-reducing agents [94]. Most interestingly, V_{Li}^0 in Li_2MnO_3 was found to be a complex of V_{Li}^- and η_{O}^+ where the latter is a hole polaron stabilized on an oxygen and bound to the former [41]. This is completely different from the structure of V_{Li}^0 found in LiMO_2 ($M = \text{Co}, \text{Ni}, \text{Mn}$) and in the vast majority of electrode materials where the hole is localized on a transition-metal ion. The implications of this on the delithiation mechanism and electronic conduction are discussed in sections 5 and 7.3.

In layered mixed transition-metal oxides such as $\text{NCM}_{1/3}$ and $\text{NCA}_{1/3}$, antisites were also reported to be common [44]. It is believed, however, that a small concentration of transition-metal antisites can be benign or even beneficial through the so-called “pillaring effect” that enhances the structural stability of layered oxides [83, 97–99]. The low formation energy of antisites in all the layered oxide materials discussed here can be ascribed in part to the small ionic-radius difference between the transition-metal ion (specifically, high-spin M^{2+} —the stable configuration of the transition-metal ions at the Li lattice site) and the Li^+ ion. However, it was also found that the formation energy has a strong dependence on the relative abundance of the host’s constituent elements in the synthesis environment, i.e., the atomic chemical potentials [36, 41, 44], as also demonstrated in this section. Systematic and comprehensive studies of defects following the computational approach outlined in section 2 are thus necessary to provide guidelines for defect characterization and defect-controlled synthesis of complex materials.

Note that, in the examples discussed in this review, the calculations were carried out for defects in the bulk. Certain defects such as transition-metal and oxygen vacancies were often found to be energetically unfavorable in the interior of the materials [36, 41, 44]. This is because the creation of these defects involves breaking the strong

transition-metal–oxygen covalent bonds which requires a high energy. At/near surfaces or interfaces, however, defects such as oxygen vacancies can have a much lower formation energy, given the less constrained lattice environment [36, 41]. It is then important to determine if non-stoichiometry observed in a given material is due to defects at the surface/interface or in the bulk. Also, even defects with high formation energies can occur with high concentrations if the material is prepared using non-equilibrium methods which can lead to excess defects being frozen in. In this case, the equilibrium concentration estimated via equation (2) should only be regarded as the lower bound.

4.2. Olivine phosphates

Iron antisites (Fe_{Li}) are often observed in LiFePO_4 . These relatively immobile defects can block the one-dimensional lithium channels and thus reduce the electrochemical performance [16, 100–102]. The antisites can occur simultaneously with other native defects. Chung *et al.* [102], for example, reported evidence of a certain amount of iron and lithium atoms exchanging sites and forming antisite pairs $\text{Fe}_{\text{Li}}\text{--Li}_{\text{Fe}}$, while Axmann *et al.* [16] found that Fe_{Li} is formed in association with lithium vacancies (V_{Li}). These conflicting reports suggest that the results can be sensitive to the actual synthesis conditions. This is, indeed, the case, as shown in a first-principles study reported in [17] which explored all defect landscapes under different conditions. The work also provided guidelines for obtaining LiFePO_4 with the lowest possible concentration of the iron antisites, which was eventually confirmed by experiments [103]. Antisite defects have also been observed in other olivine phosphates such as LiCoPO_4 [104–106] and LiNiPO_4 [107, 108].

Relevant elementary native defects in LiFePO_4 include the small hole polaron η^+ (i.e., high-spin Fe^{3+} at a Fe^{2+} lattice site; denoted as p^+ in [17] and [33]), V_{Li}^- , Li_i^+ , Fe_{Li}^+ (high-spin Fe^{2+} at a Li site), and Li_{Fe}^- (Li^+ at a Fe site). Other charge states of these defects are complexes consisting of the elementary ionic defects and polaron(s), similar to defects in layered oxides. For example, V_{Li}^0 is a complex of V_{Li}^- and η^+ , whereas Li_{Fe}^0 is a complex of Li_{Fe}^- and η^+ [17]. Different possible defect landscapes were explored by varying the atomic chemical potential values bound in slices of a polyhedron in the three-dimensional phase space in which LiFePO_4 is thermodynamically stable. One focuses on two “knobs” that can be used to tune the synthesis conditions in practice: one is the oxygen chemical potential μ_{O} , which can be controlled by controlling temperature and pressure and/or by using oxygen-reducing agents, and the other is the relative abundance of lithium in the environment, ranging from “Li-deficient” to “Li-excess” [17].

Figure 7 shows different defect landscapes in LiFePO_4 associated with different sets of the atomic chemical potentials, ranging from the lowest to highest possible μ_{O} value and from the Li-deficient to Li-excess environment, reported in [17]; for simplicity, only the lowest-energy charged defects are shown. The results were obtained in DFT+ U calculations. Lower μ_{O} values (more reducing environments) are usually associated with higher temperatures and/or lower oxygen partial pressures [equation (5)] and/or the

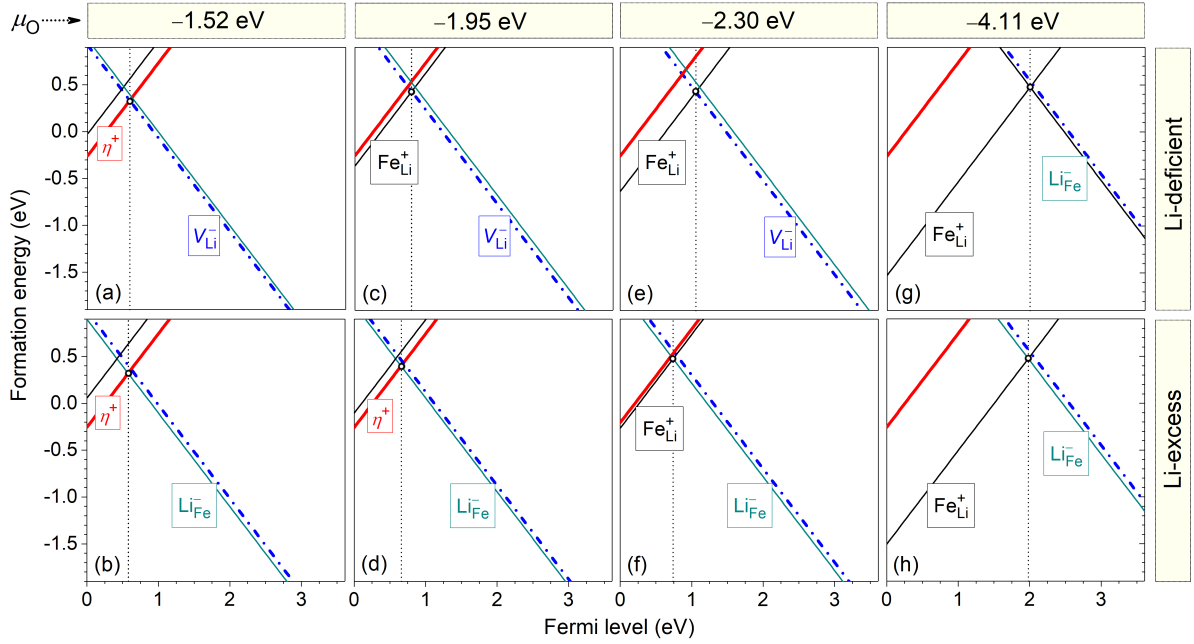


Figure 7. Formation energies of low-energy positively (η^+ , Fe_{Li}^+) and negatively (V_{Li}^- , Li_{Fe}^-) charged, elementary defects in LiFePO_4 , plotted as a function of the Fermi level from the VBM to CBM. The energies are obtained under different synthesis conditions, i.e., different μ_{O} values and in the Li-deficient or Li-excess environment. The vertical dotted line marks the Fermi-level position μ_e^{int} of the material, determined predominantly by the lowest-energy charged defects. Produced with data from [17].

presence of oxygen-reducing agents; in the extreme Li-excess (Li-deficient) environment, the system is close to forming Li-containing (Fe-containing) impurity phases [109]. The results show that Fe_{Li}^+ is the lowest-energy positively charged defect in a majority of the defect landscapes. The iron antisite can occur simultaneously with V_{Li}^- to form the neutral complex $\text{Fe}_{\text{Li}}^+-V_{\text{Li}}^-$ whose formation energy is in the range 0.36–0.56 eV, or with Li_{Fe}^- to form $\text{Fe}_{\text{Li}}^+-\text{Li}_{\text{Fe}}^-$ whose formation energy is 0.51 eV [17] (or 0.58 eV if computed using the HSE06 functional). These results are thus consistent with the experimental observation of different defect complexes reported in the literature [16, 102]. For comparison, the formation energy is 0.39 eV for the $\text{Co}_{\text{Li}}^+-\text{Li}_{\text{Co}}^-$ pair in LiCoPO_4 , 0.43 eV for the $\text{Ni}_{\text{Li}}^+-\text{Li}_{\text{Ni}}^-$ pair in LiNiPO_4 , and 0.74 eV for the $\text{Mn}_{\text{Li}}^+-\text{Li}_{\text{Mn}}^-$ pair in LiMnPO_4 ; all obtained in HSE06 calculations. The low formation energies in the case of LiCoPO_4 and LiNiPO_4 , estimated to correspond to an equilibrium concentration of about 9% for $\text{Co}_{\text{Li}}^+-\text{Li}_{\text{Co}}^-$ and 6% for $\text{Ni}_{\text{Li}}^+-\text{Li}_{\text{Ni}}^-$ when the materials are prepared at 800°C, are consistent with the high antisite defect concentrations often observed in experiments [104–108]. It should be noted that, as demonstrated in the case of LiFePO_4 , the antisite pair may not be the lowest-energy defect complex in the materials under *all* synthesis conditions.

As reported in [17], one can tune the synthesis conditions to minimize the presence of iron antisites in LiFePO_4 samples. The formation energy of Fe_{Li}^+ (at μ_e^{int}) is highest under the most oxidizing and Li-excess environment, see figure 7(b), specifically when

the formation energies of all native defects are calculated at a point on the boundary of the stability polyhedron in the three-dimensional chemical-potential phase diagram where LiFePO_4 is in equilibrium with impurity phases $\text{Li}_3\text{Fe}_2(\text{PO}_4)_3$ and Li_3PO_4 . Under these conditions, η^+ and Li_{Fe}^- are the dominant defects, and the formation-energy difference between Fe_{Li}^+ and Li_{Fe}^- is largest [17]. Note that due to the exponential dependence of the concentration on the formation energy, a small formation-energy difference will result in a large difference in the defect concentrations, especially when prepared at low temperatures. The work thus predicted specific conditions under which LiFePO_4 with a negligible concentration of iron antisites can be obtained. The prediction was eventually confirmed by Park *et al.* [103] in “lithium-excess” LiFePO_4 where Li_{Fe}^- was found to be the dominant defect and Fe_{Li}^+ has a negligible concentration. The experimental work [103] also confirmed the presence of $\text{Li}_3\text{Fe}_2(\text{PO}_4)_3$ and Li_3PO_4 as impurity phases in certain samples when fine-tuning the synthesis conditions. The excess Li occupies the Fe sites, instead of interstitial lattice sites, which is consistent with the computational results reported in [17] where the dominant defect under the mentioned synthesis conditions is Li_{Fe}^0 , i.e., Li_{Fe}^- plus η^+ . This is because lithium interstitials have a much higher formation energy than the lithium antisites [17]. As discussed in [103], the lithium excess not only suppresses the iron antisites but can also open up additional Li diffusion paths perpendicular to the one-dimensional lithium channels in the material.

4.3. Spinel-type oxides

Truly stoichiometric LiMn_2O_4 is difficult to prepare and structural defects have been reported to occur at multiple lattice sites in this spinel oxide [110–114]. Martinez *et al.* [114], for example, found about 10% of the Li ions at the Mn sites. LiMn_2O_4 samples are often made Li-overstoichiometric, either intentionally or unintentionally. The long-range charge order, expected in stoichiometric $\text{Mn}^{3+}/\text{Mn}^{4+}$ -ordered LiMn_2O_4 , is absent in Li-overstoichiometric $\text{Li}_{1+\alpha}\text{Mn}_{2-\alpha}\text{O}_4$; only short-range charge-order has been observed [115, 116]. As an electrode material, however, $\text{Li}_{1+\alpha}\text{Mn}_{2-\alpha}\text{O}_4$ shows a significantly improved cycling stability compared to stoichiometric LiMn_2O_4 [111, 117]. Note that Li-overstoichiometry also occurs in the anode material LiTi_2O_4 [118–120].

Computationally, LiMn_2O_4 is characterized by having native defects with very low formation energies. Figure 8 shows a representative defect landscape reported in [40]. As in the other electrode materials, defects in LiMn_2O_4 include elementary defects and defect complexes, and the structure and energetics of the latter can be described in terms of those of the former. The most relevant elementary defects are η^+ (i.e., Mn^{4+} at a Mn^{3+} site), η^- (high-spin Mn^{3+} at a Mn^{4+} site), V_{Li}^- , Li_i^+ , $\text{Li}_{\text{Mn}}^{2-}$ (Li^+ at a Mn^{3+} site), and Mn_{Li}^+ (high-spin Mn^{2+} at a Li site). Other charge states of the ionic defects are complexes; for example, V_{Li}^0 is a complex of V_{Li}^- and η^+ , Li_{Mn}^0 (Li_{Mn}^-) is a complex of $\text{Li}_{\text{Mn}}^{2-}$ and two (one) η^+ , and Mn_{Li}^0 is a complex of Mn_{Li}^+ and η^- . The Fermi level of LiMn_2O_4 , μ_e^{int} , is predominantly determined by the dominant positively and negatively charged defects which are always η^+ and Li_{Mn}^- . Note that LiMn_2O_4 with the $\text{Mn}^{3+}/\text{Mn}^{4+}$

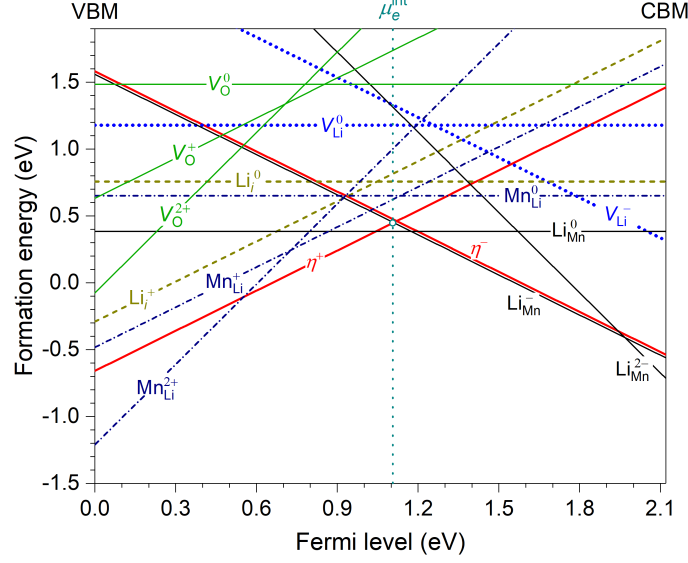


Figure 8. Formation energies of relevant native defects in LiMn_2O_4 . The energies are obtained at a point in the chemical-potential phase diagram where LiMn_2O_4 is in equilibrium with Mn_2O_3 and Li_2MnO_3 . Produced with data from [40].

ordering shown in figure 2(d) was used as the host material in the calculations, where exactly half of the Mn ions are Mn^{3+} and the other half are Mn^{4+} . The hole (electron) polaron here, η^+ (η^-), is simply an extra Mn^{4+} (Mn^{3+}) in the supercell [40].

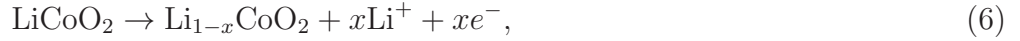
It was reported in [40] that the small polarons η^+ and η^- in LiMn_2O_4 can occur simultaneously in the form of an electron–hole polaron pair whose formation energy is only 0.37 eV. This corresponds to an estimated equilibrium concentration of about 7% at 800°C (here, $N_{\text{config}} = 4$ for the $\eta^+-\eta^-$ pair); i.e., a total of about 14% Mn^{3+} and Mn^{4+} ions are at the “wrong” Mn lattice sites with respect to the lowest-energy, $\text{Mn}^{3+}/\text{Mn}^{4+}$ -ordered model presented in figure 2(d). With such a high concentration, there would be strong $\text{Mn}^{3+}/\text{Mn}^{4+}$ disorder in real LiMn_2O_4 samples [40]. Regarding the ionic defects, the dominant defect is always the neutral complex Li_{Mn}^0 whose formation energy is only 0.11–0.38 eV. Given this result, the synthesis of LiMn_2O_4 under equilibrium or near-equilibrium conditions is expected to result in a Li-overstoichiometric compound with a high concentration of Li at the Mn site. Its chemical formula can be written as $\text{Li}[\text{Mn}_{2-\alpha}\text{Li}_\alpha]\text{O}_4$ or, more explicitly, $\text{Li}[\text{Mn}_{1-3\alpha}^{3+}\text{Mn}_{1+2\alpha}^{4+}\text{Li}_\alpha^+]\text{O}_4$; here, each negatively charged lithium antisite $\text{Li}_{\text{Mn}}^{2-}$ is charge-compensated by two hole polarons η^+ . The average Mn oxidation state in this compound is higher than +3.5 because μ_e^{int} is slightly on the left of the Fermi-level position where η^+ and η^- have equal formation energies; i.e., Mn^{4+} is slightly more favorable than Mn^{3+} . Given the $\text{Mn}^{3+}/\text{Mn}^{4+}$ disorder and the likely random distribution of Li_{Mn}^0 , long-range charge order as shown in figure 2(d) would not be realized in real LiMn_2O_4 samples [40], even at low temperatures, consistent with the experimental observations [115, 116].

It was also found that the Li^+ ion at the Mn^{3+} site, i.e., the lithium antisite, has a lower mobility and is unlikely to be deintercalated during charging [40]. Furthermore,

$\text{Li}[\text{Mn}_{2-\alpha}\text{Li}_\alpha]\text{O}_4$ has only $(1-3\alpha)$ Mn^{3+} ions for the oxidation reactions (Mn^{4+} is inactive because the oxidation to Mn^{5+} would cost too much energy). As a result, there will be residual lithium in the fully delithiated compound, at both the Li and Mn lattice sites, i.e., $\text{Li}_{3\alpha}^+[\text{Mn}_{2-\alpha}^{4+}\text{Li}_\alpha^+]\text{O}_4^{2-}$. The theoretical capacity will therefore decrease from 148 mAh/g to $148(1-3\alpha)$ mAh/g. However, in spite of that capacity loss, the presence of the residual lithium in the delithiated compound can help improve the cycling stability, unlike in stoichiometric LiMn_2O_4 where the complete extraction of lithium results in the unstable $\lambda\text{-MnO}_2$ end compound [117]. The results are thus consistent with the reports that $\text{Li}_{1+\alpha}\text{Mn}_{2-\alpha}\text{O}_4$ shows an enhanced electrochemical performance [111, 117].

5. Delithiation mechanism and extraction voltage

In lithium-ion batteries, electrode materials are subjected to lithium extraction and (re-)insertion during charge and discharge, respectively. These processes can be regarded as corresponding to the creation of *electrochemically activated* defects in the electrode materials [41]. For example, the delithiation reaction in a LiCoO_2 cathode occurs as



where the extracted Li^+ ions then dissolve into the electrolyte and the electrons move in the opposite direction to the outer circuit. The extraction of lithium (i.e., Li^+ plus e^-) from the electrode thus corresponds to the formation of lithium vacancies (V_{Li}^0) in LiCoO_2 ; here, the vacancies are electrochemically activated, as opposed to being activated thermally. In [41], it was demonstrated that the mechanism for delithiation and the extraction voltage can be obtained from the structure and energetics of V_{Li}^0 , respectively.

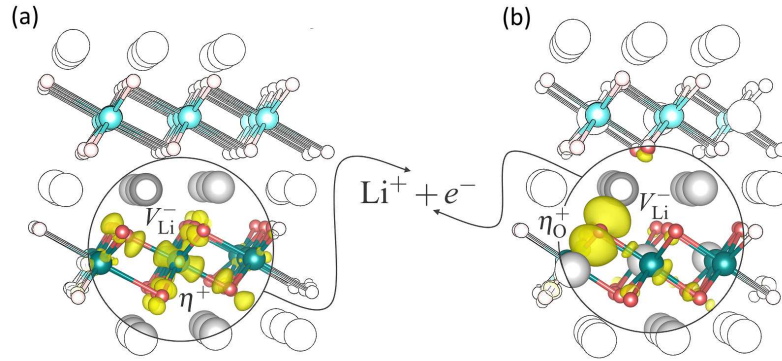


Figure 9. Mechanisms for lithium extraction in battery electrode materials, involving oxidation (a) at the transition-metal site, e.g., $\text{Mn}^{3+} \rightarrow \text{Mn}^{4+}$ in LiMnO_2 and (b) at the oxygen site, e.g., $\text{O}^{2-} \rightarrow \text{O}^-$ in Li_2MnO_3 [41]. Large (gray) spheres are Li, medium (blue) are Mn, and small (red) are O. Charge densities associated with the hole polarons η^+ (i.e., Mn^{4+}) and η_{O}^+ (i.e., O^-) are visualized as (yellow) isosurfaces.

Figure 9 shows the relationship between the structure of the V_{Li}^0 defect and the delithiation mechanism in LiMnO_2 and Li_2MnO_3 [41]. In the vast majority of electrode

materials, V_{Li}^0 is a complex of V_{Li}^- and η^+ , where the former is a void formed by the removal of a Li^+ ion from the electrode material and the latter is a hole polaron stabilized on the transition-metal ion induced by the removal of an electron from the material; see figure 9(a). In this mechanism, oxidation thus occurs on the transition-metal ion and the removal of Li^+ ions is charge compensated by the formation of hole polarons η^+ . In Li_2MnO_3 , however, V_{Li}^0 was found to be a complex of V_{Li}^- and η_{O}^+ where the latter is an oxygen-hole polaron bound to the former; see figure 9(b). In this case, the intrinsic delithiation mechanism involves the oxidation of O^{2-} to O^- ; here, charge compensation for the removal of Li^+ ions is provided by the formation of η_{O}^+ in the material [41].

The formation of η_{O}^+ bound to V_{Li}^- , as opposed to η^+ which is stable either in the presence or absence of other defects, has important implications for the performance of Li_2MnO_3 . It is known that Li_2MnO_3 is electrochemically activated at high voltages [121] and shows very limited electrochemical capacity [122]. As argued in [41] and [46], the difficulty in activating Li_2MnO_3 can be ascribed to the high extraction voltage and a lack of percolation pathways for electronic conduction in the bulk at the onset of delithiation when there are no or very few V_{Li}^- . The electrochemical performance can, however, be improved via doping with electrochemically active ions [79, 122]. The purpose of doping is to introduce additional charge compensation and electronic conduction mechanisms highly needed at the early stages of delithiation [41, 46]; see also section 7.3.

The difference in the delithiation mechanism between, e.g., Li_2MnO_3 and LiMnO_2 can be traced back to the difference in their electronic structure reviewed in section 3. This interplay between electronic structure and defect formation (and hence presence or absence and identity of active redox centers), discussed in [41], offers a simple method to computationally determine the (de)lithiation mechanism in newly discovered battery materials [123, 124] where *a priori* knowledge of the mechanism is often lacking. The relationship between electronic structure, defect structure, and functional property will also become a basis for, e.g., high-throughput computational screening and discovery of materials with certain types of cationic and/or anionic redox centers. Note that the example presented in figure 9 focuses on the initial stage of delithiation. Similar calculations and analyses can always be carried out for partially delithiated compounds to understand the delithiation mechanism at the later stages, as demonstrated in [46].

Regarding the extraction voltage, the derivation presented in [41] can be summarized as the following: From equation (3), a similar expression can be written for the formation energy of arbitrarily x lithium vacancies, $E^f(xV_{\text{Li}}^0)$, in an electrode material. During delithiation, the lithium vacancies are electrochemically activated, i.e.,

$$E^f(xV_{\text{Li}}^0) = 0, \quad (7)$$

assuming they readily form under the influence of an external power source with an extraction voltage V . Moreover, the lithium chemical potential can be expressed as

$$\mu_{\text{Li}}^* = E_{\text{tot}}(\text{Li}) - eV, \quad (8)$$

assuming equilibrium with a metallic Li anode and the external power source which acts as a reservoir of the electrons. From these expressions, the lithium-extraction voltage

can be expressed in terms of the total energies as [41]

$$V = \frac{E_{\text{tot}}(xV_{\text{Li}}^0) - E_{\text{tot}}(\text{host}) + xE_{\text{tot}}(\text{Li})}{xe}. \quad (9)$$

Here, x can take any value to describe the lithium-content difference between any two intercalation limits, and $E_{\text{tot}}(\text{host})$ can be the total energy of *any* starting composition chosen as the host material. In that case, V is the average voltage between the two limits. Expression (9) is thus equivalent to that for the average voltage derived by Aydinol *et al.* [125] who considered the electrical energy caused by charge displacement.

A similar expression for the voltage associated with lithiation can also be derived according to which the lithium-insertion process is regarded as the formation of lithium interstitials (Li_i^0) in the electrode material. The structure of Li_i^0 provides information on the lithiation mechanism [40]. Usually, one is more interested in the re-insertion of lithium into a (partially) delithiated compound. In that case, the (partially) delithiated compound should be chosen as the host material. In both delithiation and lithiation, the system is often assumed to exchange only Li^+ and e^- with reservoirs; however, it is straightforward to include other species, if needed. The general formulation presented in [41] is intuitive and can be applied to other mechanisms where lithium may not be the only extracted (inserted) species during the delithiation (lithiation) process.

6. Electronic and ionic conduction mechanisms

From the defect landscapes reported for a number of complex materials [17, 36, 40, 41, 44], including those discussed in section 4, it is clear that a change from one (nominal) defect charge state to another is associated with polaron formation, and some charged native defects have non-negative formation energies only in a small range of the Fermi-level values near midgap; see, e.g., figures 5–8. These features indicate that native point defects in these battery materials cannot act as sources of band-like holes and electrons, and the electronic conduction thus occurs via hopping of small polarons. The observed p-type (or n-type) thermally activated electronic conductivity reported in the literature should be understood as that associated with hole (electron) polarons. Also, the materials cannot be doped n- or p-type like a conventional semiconductor where the Fermi level can be at or very close to the band edges. Any attempt to deliberately shift the Fermi level to the VBM or CBM, e.g., via doping with impurities, will lead to spontaneous formation of native defects that counteract the effects of shifting, i.e., native defects act as charge-compensating centers [17]; see also section 7. Finally, the ionic conduction often occurs via migration of lithium vacancies and/or interstitials because of their higher mobility compared to other native ionic defects [17, 36, 40, 41, 44].

6.1. Defect migration energy barrier

Since defect structure and energetics have been reviewed in section 4, let us now examine defect migration, particularly the migration of small polarons and lithium vacancies.

We note that the methodology discussed in section 2 allows defect thermodynamics and kinetics to be cleanly separated so that one can easily isolate and study a defect in detail, even when it is positively or negatively charged. For the ionic defects, the energy barrier (E_m) for migration can be computed using the nudged elastic band method [69]. The migration of a small polaron between two positions q_A and q_B , on the other hand, can be described by the transfer of its lattice distortion and the migration barrier is obtained by computing the total energies of a set of supercell configurations linearly interpolated between q_A and q_B and identifying the energy maximum [14, 126, 127].

Table 1. Migration barrier E_m , in eV, of small hole (η^+) and electron (η^-) polarons and lithium vacancies via monovacancy (V_{Li}^-) and divacancy (DV_{Li}^{2-}) mechanisms.^a The transition-metal ions associated with η^+ and η^- in each compound are listed in parentheses.

	η^+		η^-		V_{Li}^-	DV_{Li}^{2-}	Ref.
LiCoO ₂	0.10	(Co ⁴⁺)	0.32	(Co ²⁺)	0.70	0.18	[36]
LiNiO ₂	0.21, 0.28	(Ni ⁴⁺)	0.26, 0.28	(Ni ²⁺)	0.56, 0.66	0.26	[36]
LiMnO ₂	0.39, 0.48	(Mn ⁴⁺)	0.30, 0.34	(Mn ²⁺)	0.58, 0.63	0.30	[41]
NCM _{1/3}	0.31 ^b	(Ni ³⁺)	0.40 ^b	(Mn ³⁺)	0.64–0.75	0.26–0.28	[44]
NCA _{1/3}	0.23 ^b	(Ni ⁴⁺)	0.30 ^b	(Ni ²⁺)	0.64–0.95	0.35–0.40	[44]
Li ₂ MnO ₃			0.33	(Mn ³⁺)	0.64, 0.82	0.29, 0.34	[41]
LiFePO ₄	0.22 (0.25)	(Fe ³⁺)			(0.32)		[17, 27]
LiMn ₂ O ₄	0.46	(Mn ⁴⁺)	0.46	(Mn ³⁺)	0.19, ^c 0.47		[40]

^a Results obtained in HSE06 calculations; only the values in parentheses are obtained in DFT+ U .

^b This work; estimated in calculations using the supercell models for LiNi_{1/3}Co_{1/3}Mn_{1/3}O₂ (NCM_{1/3}) and LiNi_{1/3}Co_{1/3}Al_{1/3}O₂ (NCA_{1/3}) and the computational details reported in [44].

^c Lithium can also migrate via an interstitialcy mechanism with an energy barrier of 0.12 eV or 0.49 eV. For both the vacancy and interstitialcy mechanisms, however, the lower barrier migration path is unlikely to be realized in (partially) Mn³⁺/Mn⁴⁺-disordered LiMn₂O₄; see more details in [40].

Table 1 lists the energy barriers for polaron and lithium-ion migration in select electrode materials. In these materials, lithium migration can occur via a (mono)vacancy mechanism, particularly V_{Li}^- . The movement of the negatively charged vacancy V_{Li}^- in one direction is equivalent to that of a Li⁺ ion in the opposite direction. In the layered oxides, lithium migration can also occur via a divacancy mechanism [23, 36], which involves a lithium divacancy DV_{Li}^{2-} (a pair of V_{Li}^-). In this mechanism, the movement of one V_{Li}^- occurs in the presence of the other V_{Li}^- . The monovacancy mechanism is expected to be dominant in nearly fully lithiated compounds, i.e., when the concentration of lithium vacancies is low; the divacancy mechanism is dominant in partially delithiated layered oxides where the concentration of lithium vacancies is high, i.e., when DV_{Li}^{2-} has a low formation energy [36, 41, 44]. Note that the calculated migration barriers reported in the literature by other research groups may often be those for neutral vacancies V_{Li}^0 which, as discussed in section 4, actually have two components: V_{Li}^- and a hole polaron.

6.2. Conductivity and activation energy

The activation energy for conduction associated with a defect can be estimated from its formation energy and migration barrier. Care should be taken, however, when making direct comparisons with the activation energy obtained in experiments. The following discussion, based on that presented in [36] and [81], is general and applicable to any materials with defect-mediated, thermally activated electronic and/or ionic conduction.

The conductivity associated with a current-carrying defect can be defined as

$$\sigma = qmc, \quad (10)$$

where q , m , and c are the defect's charge, mobility, and concentration, respectively. The mobility is assumed to be thermally activated, i.e.,

$$m = m_0 \exp\left(-\frac{E_m}{k_B T}\right), \quad (11)$$

where $m_0 \propto 1/T$ [128] is a pre-exponential factor. The concentration c , on the other hand, can include both thermally activated and athermal defects [36, 81],

$$c = c_a + c_t = c_a + c_0 \exp\left(-\frac{E^f}{k_B T}\right), \quad (12)$$

where c_a is the athermal concentration consisting of defects that, e.g., preexist in the material before the conductivity measurements, c_t is the concentration of defects that are thermally activated during the measurements at finite temperatures, and c_0 is a pre-exponential factor. In general, the E^f value that enters equation (12) will not necessarily be the same as that calculated using a specific set of conditions under which the material is prepared. This is because the experimental conditions (and hence the atomic chemical potential values) during the synthesis are generally different from those during the conductivity measurements. Exceptions are cases in which the current-carrying defects are formed via, e.g., a Frenkel or full-Schottky defect mechanism or an electron–hole polaron pair mechanism (e.g., polarons in LiNiO_2 and LiMn_2O_4 , see section 4) and thus the defect formation energy is independent of the chemical potentials. The range of defect formation energy values calculated within the allowed range of the chemical potentials (sections 2 and 4) is, however, still useful, assuming that the host compound is stable during the conductivity measurements and thus the atomic chemical potentials are still subject to the same thermodynamic constraints regarding phase stability.

From equations (10)–(12), it is clear that when the athermal defects are dominant, i.e., $c_a \gg c_t$, the observed temperature-dependence of the conductivity will show an activation energy that includes only the migration barrier, i.e.,

$$E_a = E_m; \quad (13)$$

when the thermally activated defects are dominant, i.e., $c_t \gg c_a$, the activation energy will include both the formation energy and migration barrier, i.e.,

$$E_a = E^f + E_m. \quad (14)$$

The $c_a \gg c_t$ and $c_t \gg c_a$ situations correspond to the “extrinsic” (low-temperature) and “intrinsic” (high-temperature) regions, respectively, joined by a *convex* knee as often shown in Arrhenius plots of $\ln(\sigma T)$ vs. $1/T$. As far as the defect concentration is concerned, *the effective activation energy for conduction is thus dependent on the c_a/c_t ratio*; the conductivity is, on the other hand, dependent on the total concentration ($c_a + c_t$) as seen in equation (10).

Note that defect association, not included in the above equations, may have an impact on the conductivity and the activation energy at lower temperatures. In that case, the activation energy includes the migration barrier plus the energy needed to separate the defects, and in the $\ln(\sigma T)$ vs. $1/T$ plot there is usually a *concave* knee between the region with the associated defects and that with dissociated ones [128].

In battery electrode materials, athermal defects (c_a) may include native defects that occur during the synthesis and get trapped in materials, including those that act as charge-compensation centers in materials doped with electrically active impurities (see section 7), and electrochemically activated positively charged (i.e., hole) polarons and negatively charged lithium vacancies in partially delithiated compounds (see section 5). These defects, particularly those that contribute to charge transport, can act as preexisting current-carrying defects in subsequent conductivity measurements.

6.3. Interpretation of conductivity data

Let us now illustrate the earlier discussion with a few examples, using the conductivity data^{||} available in the literature. The activation energy for electronic conduction was reported to be 0.11–0.16 eV in “ $\text{Li}_{1.0}\text{CoO}_2$ ” and 0.11 eV in $\text{LiCo}_{0.97}\text{Mg}_{0.03}\text{O}_2$ [129, 130]. Nobili *et al.* [131, 132] found the activation energy in Li_xCoO_2 drops from about 0.4 eV for $x \sim 1$ to 0.1 eV for $x \sim 0.9$. These values, particularly those for $x < 1$ (but still larger than the lithium content at which occurs the insulator–metal transition) and in the Mg-doped samples, are almost identical to the calculated migration barrier, 0.10 eV, of η^+ in LiCoO_2 [36]. This indicates that $c_a(\eta^+) \gg c_t(\eta^+)$ during the measurements of these samples and thus $E_a \sim E_m$. The athermal η^+ can exist as the charge-compensating defect of V_{Li}^- in the partially delithiated samples or of MgCo^- in the Mg-doped samples (see also section 7). Even the so-called “ $\text{Li}_{1.0}\text{CoO}_2$ ” can have $c_a \gg c_t$, as indicated by the reported low activation energy [129]. Lin *et al.* [133], on the other hand, found much larger activation energies, 0.97–1.23 eV, in single crystals of stoichiometric LiCoO_2 grown by a vapor transport method. Here, the crystals must have very few preexisting η^+ defects and η^+ needs to be thermally activated during the measurements, according to which $c_t \gg c_a$. Indeed, the measured activation energies agree well with the range of values, 0.99–1.69 eV, calculated from the formation energies and migration barrier of η^+ reported in [36]. The $E_a = 0.4$ eV value reported for some LiCoO_2 samples [131, 134] is

^{||} In many experimental reports, the activation energy may be incorrectly derived from the slope of a $\ln(\sigma)$ vs. $1/T$ plot, instead of a $\ln(\sigma T)$ vs. $1/T$ plot as it should be for *thermally activated* electronic and ionic conduction [Note the pre-factor $m_0 \propto 1/T$ in equation (11) for the mobility]. In that case, the *actual* activation energy may be larger than the reported value, usually by about a few percent.

closer to E_m than to $E^f + E_m$ [36], suggesting a high c_a/c_t ratio, though it is expected to be much lower than that in some samples mentioned above. As for the ionic conduction, Wang *et al.* [134] reported an activation energy of 0.57 eV in LiCoO_2 , which is close to the energy barrier for lithium migration via the monovacancy mechanism [36]; see also Table 1. This suggests that $c_a \gg c_t$ for V_{Li}^- in this case, though the total concentration ($c_a + c_t$) of V_{Li}^- is too small to make the divacancy mechanism favorable. Indeed, Wang *et al.*'s "almost stoichiometric" LiCoO_2 sample shows very low electronic and ionic conductivities [134], which indicates very low concentrations of η^+ and V_{Li}^- , especially given the fact that η^+ is highly mobile (i.e., has a very low migration barrier) [36].

In the case of LiNiO_2 , it should be noted there is already a significant concentration of preexisting (athermal) η^+ and η^- defects; see section 4.1. In principle, both the hole and electron polarons can contribute to the electronic conductivity. However, since LiNiO_2 samples may often be Li-deficient, e.g., due to Li loss during the synthesis and/or when being partially delithiated, η^+ would have a higher concentration. In addition, the migration barrier of η^+ is slightly smaller than that of η^- ; see Table 1. As a result, η^+ is likely the majority charge-carrying species in the electronic conduction. Indeed, Seebeck coefficients were reported to be positive in LiNiO_2 samples (for $T < 300$ K) [135]. Molenda *et al.* [135] found activation energy values of 0.14–0.19 eV (± 0.02 eV), which are in good agreement with the calculated migration barrier (as low as 0.21 eV) of η^+ in LiNiO_2 [36]. In the partially delithiated Li_xNiO_2 ($0.6 \leq x < 1.0$), the activation energy only decreases slightly (which may be ascribed to the lattice parameter changes) [135], again indicating $c_a \gg c_t$ for polarons even in the (nominal) $\text{Li}_{1.0}\text{NiO}_2$ sample.

The above discussion also serves as a basis for understanding LiNiO_2 -related mixed transition-metal materials, especially Ni-rich layered oxides, where the electronic conduction is largely determined by the Ni ions. The valence-band top of these materials is predominantly composed of the Ni 3d states; as a result, Ni^{2+} and Ni^{3+} are oxidized before any other transition-metal ions (e.g., Co^{3+}) and small polarons associated with the Ni ions dominate the electronic transport in lithiated and partially delithiated compounds; see, e.g., the electronic structure and voltage profiles of $\text{NCM}_{1/3}$ and $\text{NCA}_{1/3}$ reported in [44]. Experimentally, Saadoune and Delmas [136] reported activation energy values for electronic conduction in $\text{Li}_x\text{Ni}_{0.8}\text{Co}_{0.2}\text{O}_2$ varying from 0.22 eV ($x = 1.0$) to 0.17 eV ($x = 0.65$), in the 220–290 K range. In $\text{Li}_{1-x}\text{Ni}_{0.8}\text{Co}_{0.15}\text{Al}_{0.05}\text{O}_2$, often referred to as "NCA" in the literature, Amin *et al.* [137] reported a range of activation energy values, 0.22–0.14 eV (± 0.04 eV) for $x = 0$ –0.60. In other materials such as Ni-rich NMC, $\text{LiNi}_{1-x-y}\text{Mn}_x\text{Co}_y\text{O}_2$, the activation energy was reported to be 0.24 eV (NMC811), 0.27 eV (NMC622), or 0.29 eV (NMC532) [134]. All these values are in good agreement with the calculated migration barrier (0.21–0.31 eV) of small polarons associated with the Ni ions in LiNiO_2 , $\text{NCM}_{1/3}$, and $\text{NCA}_{1/3}$; see Table 1. This indicates that $c_a \gg c_t$ in these samples and $E_a \sim E_m$. Amin and Chiang [138] reported a slightly larger activation energy, 0.42 eV, for lithiated NMC532, which suggests a lower c_a/c_t ratio for polarons in their sample. The activation energy, however, decreases quickly for $x > 0$ [138], as expected. Note that, in samples with high delithiation states, η^+ associated with

Co^{4+} can contribute to the electronic transport; the migration barrier of this polaron in LiCoO_2 is only 0.10 eV [36].

Like in the Ni-rich NMC materials, the electronic conduction in NMC333 (i.e., $\text{NCM}_{1/3}$) at high lithiation states is also characterized by that in LiNiO_2 due to the similarity in the nature of the valence-band top of the two compounds [36, 44]. Hole polarons η^+ in $\text{Li}_{1-x}\text{Ni}_{1/3}\text{Co}_{1/3}\text{Mn}_{1/3}\text{O}_2$ are predominantly Ni^{3+} for $0 < x \leq 1/3$, Ni^{4+} for $1/3 < x \leq 2/3$, or Co^{4+} for $2/3 < x \leq 1$, as evidenced in the voltage profile reported in [44]. The migration barrier of η^+ associated with Ni^{3+} is calculated to be 0.31 eV. Experimentally, Wang *et al.* [134] found an activation energy of 0.36 eV in lithiated NMC333 whereas Amin and Chiang [138] reported a value of 0.48 eV (± 0.03 eV). The activation energy then decreases quickly as a function of x , from 0.29 eV ($x = 0.1$) to 0.10 eV ($x = 0.75$) [138], similar to what was observed in, e.g., NMC532 [138] mentioned above. These values are comparable to the calculated migration barriers (0.21–0.31 eV) of hole polarons associated with Ni^{3+} and Ni^{4+} in LiNiO_2 [36], $\text{NCM}_{1/3}$, and $\text{NCA}_{1/3}$ or that (0.10 eV) of hole polarons associated with Co^{4+} in LiCoO_2 [36]; see Table 1. This indicates that, in the vast majority of NMC333 samples mentioned here, $c_a(\eta^+) \gg c_t(\eta^+)$ and $E_a \sim E_m$. Also, the electronic conductivity in lithiated NMC333 is often reported to be very low [138, 139] compared to that in the partially delithiated NMC333 samples, indicating a low total concentration ($c_a + c_t$) of polarons in the lithiated samples.

Regarding the ionic conduction in the NMC and NCA materials, Wang *et al.* [134] reported an activation energy of 0.27 eV for NMC333, in excellent agreement with the lithium migration barrier via a divacancy mechanism, 0.26–0.28 eV, reported in [44]. The activation energies in other compounds are 0.25 eV (NMC532), 0.22 eV (NMC622), and 0.14 eV (NMC811) [134], also comparable to the lithium migration barriers via a divacancy mechanism in the layered oxides as summarized in Table 1. This indicates that the samples investigated by Wang *et al.* all have $c_a \gg c_t$ for V_{Li}^- and thus $E_a \sim E_m$, and $c_a + c_t$ is high enough that lithium divacancies are energetically favorable and the divacancy migration mechanism becomes dominant. The total concentration of lithium vacancies in the NMC333 sample is, however, expected to be smaller than that in the Ni-rich samples, given NMC333's much lower ionic conductivity [134]. Note that Amin *et al.* [137] reported a much higher activation energy, 1.25 eV, for ionic conduction in $\text{Li}_{1-x}\text{Ni}_{0.8}\text{Co}_{0.15}\text{Al}_{0.05}\text{O}_2$ with $x = 0$. In this case, the material must have $c_t \gg c_a$ for V_{Li}^- and the activation energy includes both the formation energy and migration barrier.

For LiFePO_4 , Molenda *et al.* [140] reported an activation energy of 0.66 eV for the electronic conduction, comparable to that of 0.65 ± 0.05 eV reported by Zaghib *et al.* [141] and 0.55–0.59 eV by Amin *et al.* [142]. Since the calculated migration barrier of η^+ in LiFePO_4 is only 0.17–0.25 eV [17, 26, 27], the measured activation energy must include both the formation and migration energies, i.e., η^+ is thermally activated and $c_t \gg c_a$. Indeed, an estimation using the lowest calculated formation energy, 0.32 eV, of η^+ gives $E_a = 0.57$ eV [17]. We note that, in the “ $\log(\sigma)$ ” vs. $1/T$ plot reported in [141], there appears to be a convex knee at the low- T end which suggests the reported activation energy is in the intrinsic region, i.e., $E_a = E^f + E_m$. Regarding the ionic conduction,

the activation energy was reported to be in the range 0.62–0.74 eV [140, 142]. These values are close to the activation energy, 0.65 eV, associated with the formation and migration of V_{Li}^- , estimated using the lowest calculated formation energy [17].

Finally, LiMn_2O_4 is another interesting case where the concentrations of athermal polarons are already very high because (slightly more than) half of the Mn ions in the material are Mn^{4+} (i.e., η^+) and the rest are Mn^{3+} (η^-); see section 4.3. As a result, the activation energy for electronic conduction $E_a \sim E_m = 0.46$, the migration barrier of η^+ and η^- [40]. The result is in excellent agreement with the experimental values, 0.40–0.44 eV, reported in the literature [143–145]. As for the ionic conduction, the activation energies associated with the vacancy mechanism (V_{Li}^-) in the extrinsic and intrinsic regions are 0.47 and 1.11 eV, respectively; the values associated with the interstitialcy mechanism (Li_i^+) are 0.49 and 1.25 eV [40]. Experimentally, Takai *et al.* [146] reported activation energies of 0.52 and 1.11 eV for lithium diffusion below and above 600°C.

7. Theory of doping in complex materials

Doping with impurities has been a widely used method to optimize the properties and performance of battery materials. First-principles defect calculations can provide a detailed understanding of its effects and identify potentially new and effective dopants. In the calculations, supercell models with different cell sizes can be used to describe a range from lightly to heavily doped materials; they may contain an isolated impurity or a complex consisting of impurities or impurities and native defects. From a materials modeling perspective, lightly doped compounds can effectively serve as model systems for understanding more complex, mixed-metal materials [33, 45, 46]. In this section, we discuss the lattice site preference and defect structure of select transition-metal and non-transition-metal impurities in a number of battery electrode materials and the effects of doping on the electronic and ionic conduction and the delithiation mechanism.

7.1. Lattice site preference and defect structure

The most important task in the study of doping is to determine the lattice site preference of impurities (dopants), i.e., where the impurities are located in the host lattice when the material is prepared under certain conditions. In LiCoO_2 , for example, a substitutional impurity X, where X is a metal, can stay at either the Li site or the Co site (The impurity is expected to be energetically unfavorable at an interstitial site). The lattice site preference can be quantified by considering the formation-energy difference [33, 45]

$$\Delta E = E^f(\text{X}_{\text{Li}}^{q1}) - E^f(\text{X}_{\text{Co}}^{q2}), \quad (15)$$

where $E^f(\text{X}_{\text{Li}}^{q1})$ and $E^f(\text{X}_{\text{Co}}^{q2})$ are the formation energies (at μ_e^{int}) of the lowest-energy configurations of X at the Li and Co sites. Here, $\Delta E > 0$ indicates that the impurity X is energetically more favorable at the Co site than the Li site, whereas $\Delta E \sim 0$ means it can be incorporated on both lattice sites with comparable concentrations.

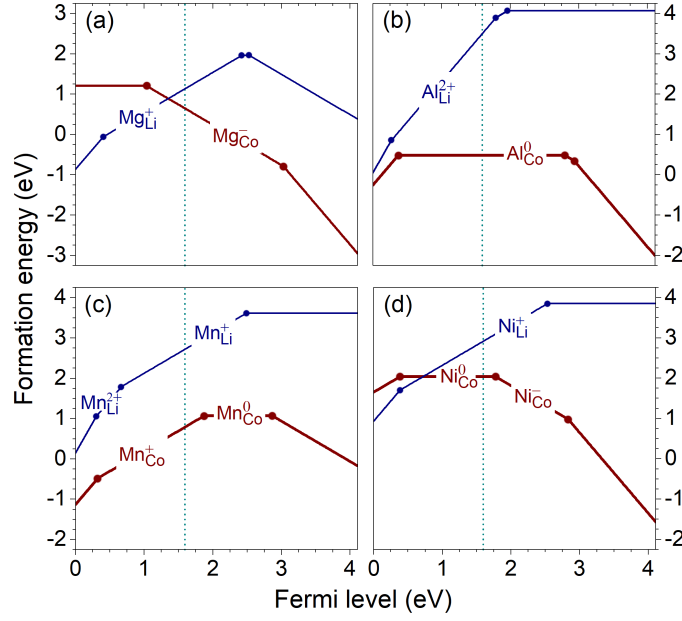


Figure 10. Relative formation energies of substitutional (a) Mg, (b) Al, (c) Mn, and (d) Ni at the Li and Co sites in LiCoO_2 obtained at point M in the chemical-potential phase diagram (figure 1), plotted as a function of the Fermi level from the VBM to the CBM of the undoped compound. For each defect, only the true charge states are indicated. The vertical dotted line marks the Fermi level of undoped LiCoO_2 , μ_e^{int} , determined by the native defects (figure 5). Produced with data from [45].

Let us illustrate with an example. Figure 10 shows the formation energies of select substitutional impurities in LiCoO_2 for a given set of the chemical potentials [45]. Specifically, the results were obtained at point M in the chemical-potential phase diagram where the Fermi level of the host material is at μ_e^{int} (see figure 5). Under these conditions, all the impurities are energetically more favorable at the Co site, as Mg_{Co}^- (i.e., Mg^{2+}), Al_{Co}^0 (Al^{3+}), Mn_{Co}^+ (Mn^{4+}), and Ni_{Co}^0 (low-spin Ni^{3+}). Some impurities are thus charged and some are neutral; the charged configurations can combine with native defects to form neutral defect complexes [45]. Of course, the results presented in figure 10 are not the only scenario that may occur. One should note that μ_e^{int} is dependent on the atomic chemical potentials of the host compound's constituent elements; as a result, the most stable charge and spin states of the impurities as well as the formation-energy difference ΔE are also dependent on the atomic chemical potentials. A systematic investigation of the impurities in LiCoO_2 shows that Al, Fe, and Mn are more favorable at the Co site in LiCoO_2 , whereas Mg and Ni can be incorporated at the Co and/or Li sites depending on the synthesis conditions. For detailed results of the lattice site preference and defect structure of impurities in LiCoO_2 , LiNiO_2 , and LiMnO_2 , see [45].

In another example [46], substitutional impurities Al, Fe, Mo, and Ru were found to be energetically most favorable when incorporated into Li_2MnO_3 at the Mn site, whereas Mg is most favorable at the Li sites. Interestingly, Ni can be incorporated at the Li site as Ni_{Li}^+ (i.e., Ni^{2+} at the Li ($2b$) site) and/or the Mn site as Ni_{Mn}^- (low-spin Ni^{3+} at the

Mn site), and the distribution of Ni over the lattice sites can be tuned by tuning the synthesis conditions. More interestingly, when two Ni atoms are incorporated at the Li (2b) site and one at the Mn site, the impurities occur as a complex of two Ni_{Li}^+ and one $\text{Ni}_{\text{Mn}}^{2-}$, i.e., all the Ni ions are in the +2 charge state [46]. The results for Ni provide an explanation for the existence of the series of Ni-doped Li_2MnO_3 cathode materials, $\text{Li}[\text{Ni}_x\text{Li}_{1/3-2x/3}\text{Mn}_{2/3-x/3}]\text{O}_2$ ($0 \leq x \leq 1/2$), synthesized first by Lu *et al.* [147, 148] and widely studied experimentally. This example thus illustrates how charge and spin states of a transition-metal impurity can be affected by defect–defect interaction [46].

Effects of co-doping were also investigated with particular attention paid to direct impurity–impurity interaction [45]. In (Ni,Mn)-doped LiCoO_2 , for example, the dopants were found to be stable as Ni_{Co}^- (i.e., Ni^{2+}) and Mn_{Co}^+ (Mn^{4+}), whereas the dopants in (Ni,Al)-doped LiCoO_2 are stable as Ni_{Co}^0 (i.e., low-spin Ni^{3+}) and Al_{Co}^0 (Al^{3+}). The Ni–Mn interaction on the Co sublattice thus leads to charge transfer between the dopants. Co-doping of LiNiO_2 with Co and Mn results in the formation of Co_{Ni}^0 (i.e., low-spin Co^{3+}), Mn_{Ni}^+ (Mn^{4+}), and η^- (Ni^{2+}); in (Co,Al)-doped LiNiO_2 , the defect structures are Co_{Ni}^0 and Al_{Ni}^0 . Similarly, co-doping of LiMnO_2 with Ni and Co leads to the formation of Ni_{Mn}^- (i.e., Ni^{2+}), Co_{Mn}^0 (low-spin Co^{3+}), and η^+ (Mn^{4+}). These co-doped systems as well as the singly doped ones discussed earlier can serve as model systems for understanding the commercially available $\text{LiNi}_x\text{Co}_y\text{Mn}_z\text{O}_2$ (NCM or NMC) and $\text{LiNi}_x\text{Co}_y\text{Al}_z\text{O}_2$ (NCA), where $x+y+z = 1$ [45]. Nickel-rich layered oxides, for example, can be understood based on the results for the undoped and doped LiNiO_2 systems; see also [45] for a discussion of Co-rich $\text{LiCo}_{1-2x}\text{Ni}_x\text{Mn}_x\text{O}_2$ where the observed charge states of the impurities were explained using the results for singly doped and co-doped LiCoO_2 . For a discussion of electronic and ionic transport in NMC and NCA materials, see section 6.3.

Overall, comprehensive studies of doping in battery materials reported in [33], [45], and [46] show that the lattice site preference of impurities does not simply depend on the ionic-radius difference between the dopant and the substituted host atom, but also on the relative abundance of the host compound’s constituent elements in the synthesis environment. For transition-metal impurities, the lattice site preference also depends on the dopant’s charge and spin states which are coupled strongly to the local lattice environment and can be strongly affected by the presence of co-dopant(s). These studies also provide low-energy defect models for various doped systems which are useful for experimental analyses of the materials and essential to the calculations of the electronic structure and investigations of the delithiation mechanism; see also section 7.3.

7.2. Manipulation of charged native defects

As discussed in section 6, native defects in the electrode materials discussed here cannot act as sources of band-like carriers and the materials cannot really be doped n- or p-type like a conventional semiconductor, at least in the dilute doping limit. In [33], it is argued that rather than generating band-like carriers, “doping” should be understood as manipulating the concentration of native defects. As far as the defect concentration

is concerned, there are two (interrelated) effects. One is the charge-compensation effect that occurs during the synthesis of the doped material. As reviewed in section 7.1, impurities when introduced into the material can be positively or negatively charged and behave as donor-like or acceptor-like dopants, respectively. These electrically active impurities will promote the formation of native defects with the opposite charge to maintain charge neutrality. Both the impurities and the native defects get “frozen in” and will act as athermal, preexisting defects in subsequent material use or measurements. The second effect involves the shift of the Fermi-level position as the charge neutrality condition is re-established in the presence of the electrically active impurities; see below.

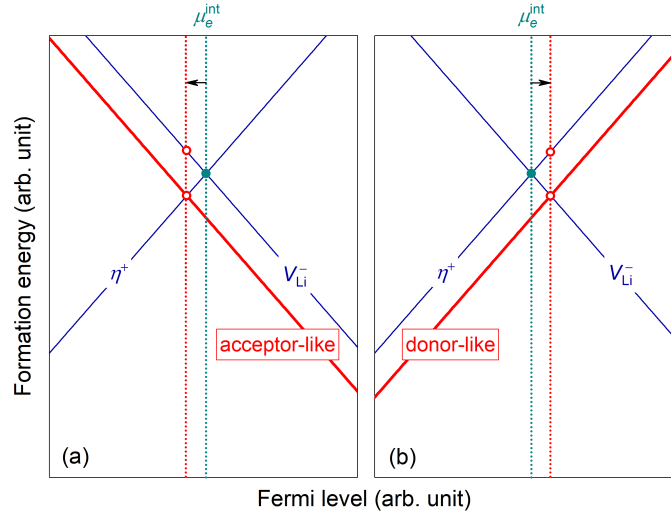


Figure 11. Schematic illustrations of (a) acceptor-like and (b) donor-like doping in a battery electrode material. η^+ and V_{Li}^- are assumed to be the dominant native defects which determine the Fermi level μ_e^{int} of the undoped material. If incorporated with a concentration higher than that of V_{Li}^- , an acceptor-like impurity will shift the Fermi level from μ_e^{int} toward the VBM, thus decreasing (increasing) the formation energy of η^+ (V_{Li}^-). For a donor-like impurity, the Fermi level will be shifted toward the CBM, thus decreasing (increasing) the formation energy of V_{Li}^- (η^+); see also [33].

Figure 11 illustrates how the Fermi level gets shifted and the formation energy of η^+ and V_{Li}^- is modified in the case of acceptor- and donor-like doping. Because the activation energy associated with η^+ (V_{Li}^-) in the intrinsic region contains the defect’s formation energy (see section 6), it will be decreased or increased accordingly and the change can be observed in the measured electronic (ionic) conductivity. It should be noted that, though η^+ and V_{Li}^- are emphasized in this example, the above analysis holds for any other positively or negatively charged native defects, including those that do not participate in mass and charge transport in the material. Similar argumentation related to Fermi-level shifting has also been developed to understand the decomposition and dehydrogenation reaction kinetics in hydrogen storage materials [149–151] and the kinetics of reduction and (re-)oxidation reactions in solid-oxide fuel cell materials [64].

Let us now analyze the conductivity data for some doped battery materials in light of the above argumentation and the available computational results. Layered

LiCoO₂ doped with Mg has been shown to enhance the electronic conductivity [130,132]. Magnesium in LiCoO₂ is stable as Mg_{Co}⁻ and charge-compensated by η^+ (i.e., Co⁴⁺) [45]; i.e., the incorporation of the acceptor-like Mg_{Co}⁻ leads to the formation of η^+ with an equal amount. Levasseur *et al.* [130] reported an activation energy of 0.11 eV in Li_{1.0}Co_{0.97}Mg_{0.03}O₂, compared to 0.16 eV in “Li_{1.0}CoO₂”. The value for the Mg-doped sample is almost identical to the migration barrier of η^+ (0.10 eV) [36], indicating the concentration of preexisting η^+ defects in the doped sample is high enough so that $c_a \gg c_t$ and the activation energy contains only the migration part; see section 6.

The second example involves Al-doped LiFePO₄. Here, Al is stable as Al_{Fe}⁺, i.e., donor-like, and charge-compensated by V_{Li}⁻ [33]. Amin *et al.* [152] reported activation energy values of 0.15 eV and 0.65 eV (along the *c*-axis) below and above a *convex* knee in the “log(σ)” vs. 1/*T* plot, compared to 0.55 eV in the undoped sample [142]. The lower value is comparable to the migration of η^+ and this region can thus be interpreted as having $E_a \sim E_m$; i.e., $c_a \gg c_t$ at low temperatures. The higher value is higher than that for the undoped sample, which can be interpreted as $E_a = E^{f,*} + E_m$, where $E^{f,*}$ ($> E^f$) is the formation energy of η^+ that is increased due to rightward shift of the Fermi level; see figure 11(b). Regarding the ionic conduction, Amin *et al.* [153] reported values of 1.04 eV and 0.46 eV (along the *b*-axis) below and above a *concave* knee in the “log(σ)” vs. 1/*T* plot, compared to 0.62 eV in the undoped [142]. The lower value is comparable to the migration barrier (0.32 eV) of V_{Li}⁻ [17] and can be interpreted as being in the extrinsic region. The higher value likely includes the migration barrier plus the dissociation energy; i.e., the system is in the region where V_{Li}⁻ is bound to Al_{Fe}⁺.

7.3. Modification of the delithiation mechanism

Let us now illustrate the effects of doping on the delithiation mechanism and extraction voltage in the electrode materials by using Li₂MnO₃, a battery material with anionic electrochemical redox activity, as an example. Figure 12 shows the calculated voltage profiles of the undoped and Li₂MnO₃ heavily doped with Ni, Mo, or Ru reported in [46]. The compositions considered here include Li₂Mn_{1-z}Ni_zO₃ with Ni stable as Ni⁴⁺ at the Mn site, i.e., Ni_{Mn}⁰; Li_{2-z}Ni_zMnO₃ with Ni stable as Ni²⁺ at the Li (2*b*) site, i.e., Ni_{Li}⁺, and charge compensated by η^- (i.e., Mn³⁺); Li_{2-2z}Ni_{3z}Mn_{1-z}O₃ or, equivalently, Li[Ni_yLi_{1/3-2y/3}Mn_{2/3-y/3}]O₂, with one Ni at the Mn site (Ni_{Mn}²⁻) for every two Ni at the Li (2*b*) site, all stable as Ni²⁺; Li₂Mn_{1-z}Mo_zO₃ with Mo stable as Mo⁵⁺ at the Mn site, i.e., Mo_{Mn}⁺, and charge compensated by η^- ; and Li₂Mn_{1-z}Ru_zO₃ with Ru stable as Ru⁴⁺ at the Mn site, i.e., Ru_{Mn}⁰; $z = y/2 = 1/4$ in all cases. These systems were built based on the lattice site preference of the impurities determined from first principles [46].

Clearly, doping can introduce additional delithiation mechanisms. In the examples presented in figure 12, they are the conventional mechanisms which involve oxidation on the transition-metal ion, as opposed to the intrinsic, oxygen-oxidation mechanism of the undoped Li₂MnO₃. The dopants are electrochemically active, except in the case of Li₂Mn_{1-z}Ni_zO₃; in some cases, the impurity–host interaction also turns some inactive

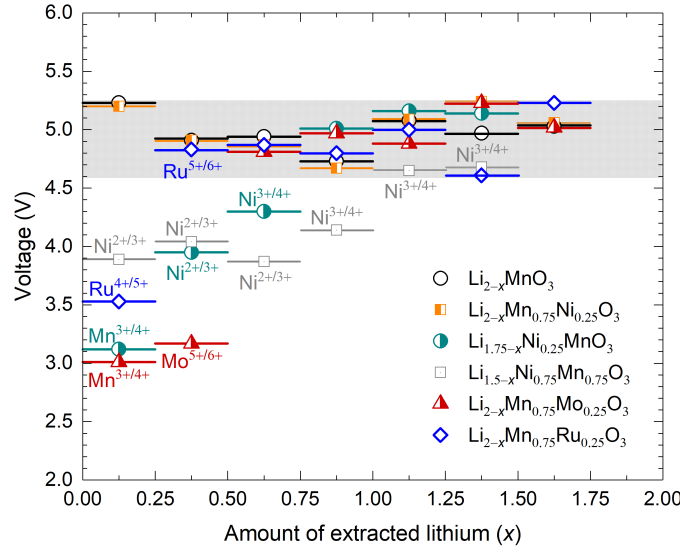


Figure 12. Voltage profiles of undoped Li_2MnO_3 and Li_2MnO_3 doped with Ni, Mo, or Ru at different lattice sites; see the text. The redox couples associated with different voltage points are indicated; unmarked voltage points in the shaded area are those associated with the redox activity on oxygen. Reprinted with permission from [46].

Mn^{4+} ions of the host into Mn^{3+} which are then oxidized during lithium extraction. Charge compensation and bulk electronic conduction in the initial stages of delithiation of the doped materials are thus provided by the electrochemically active transition-metal ions. The lower voltages associated with these non-oxygen redox couples also make it easier for lithium removal. The mechanism involving the $\text{O}^{2-/-}$ redox couple is expected to be more efficient in the later stages of delithiation where the concentration of V_{Li}^- is high and hence bulk electronic transport via η_{O}^+ may become possible [41].

Finally, it should be noted that there appears to be uncertainties and conflicting reports in the literature regarding the exact nature of the oxidized oxygen species involved in the delithiation of Li_2MnO_3 -based and related materials, i.e., whether it is O^- (i.e., η_{O}^+ in the defect notation [41]) or peroxide-like O_2^{2-} [78, 79, 122, 154–156]. Tarascon and co-workers, for example, appeared to conclude that the species is O_2^{2-} , at least in the Ru-based systems such as $\text{Li}_2\text{Ru}_{1-y}\text{Sn}_y\text{O}_2$ [154] and $\text{Li}_2\text{Ru}_{1-y}\text{Ti}_y\text{O}_2$ [155]. Bruce and co-workers, on the other hand, found evidence of “localized electron holes on oxygen” but little or no evidence for the formation of true O_2^{2-} species in $\text{Li}[\text{Li}_{0.2}\text{Ni}_{0.2}\text{Mn}_{0.6}]\text{O}_2$ [78], i.e., $\text{Li}[\text{Ni}_y\text{Li}_{1/3-2y/3}\text{Mn}_{2/3-y/3}]\text{O}_2$ with $y = 1/5$, and $\text{Li}_{1.2}[\text{Ni}_{0.13}\text{Co}_{0.13}\text{Mn}_{0.54}]\text{O}_2$ [79], which is consistent with the computational results for undoped and doped Li_2MnO_3 reported in [41] and [46]. The difference could be due to the strong Ru-O interaction, including the strong hybridization between the η_{O}^+ 2p and Ru 4d states, as observed in Ru-doped Li_2MnO_3 compared to the Ni- or Mo-doped systems [46]. It is possible that oxidized oxygen species other than or in addition to O^- can form in Li_2MnO_3 -related materials with a high Ru content and/or at very high degrees of delithiation where the lattice environment can be drastically different from the layered structure of the lightly

delithiated compounds. Comparative experimental studies of, e.g., Ni- or Mo-doped vs. Ru-doped Li_2MnO_3 or similar systems could shed more light on this issue.

8. Conclusions and outlook

We have described a theoretical framework based on defect physics that is able to provide a detailed understanding of complex energy materials. Through examples involving complex oxide and polyanionic compounds, we have demonstrated that the approach is effective in predicting defect landscapes under different synthesis conditions, providing guidelines for defect characterization and defect-controlled synthesis, uncovering the mechanisms for electronic and ionic conduction and electrochemical extraction and (re-)insertion, and providing an understanding of the effects of doping. The materials were also found to exhibit a rich defect physics resulting from the ability of the transition-metal ions to exist in different charge and spin states and the strong coupling between charge, spin, and local atomic structure. Although the examples involve battery materials, the approach and the underlying physical principles discussed here are applicable to other classes of materials. In general, the approach can be applied to any materials in which the defect physics drives the properties of interest.

The power of the theoretical and computational approach described in this review comes in part from systematic first-principles defect studies. These studies, in turn, could benefit from a certain level of automation, from setting up the calculations to processing the results. The energy landscapes in materials such as those for battery electrodes are, however, very complex and the system containing defects can easily be trapped in a local minimum. The computational tools and algorithms, therefore, have to be very robust to ensure that the obtained defect configurations are indeed the ground state. The data generated from such high-throughput first-principles defect calculations could then be used in the construction of an interactive database for defects in solids and in further studies using data-driven approaches to materials screening and discovery.

The equilibrium conditions with impurity phases often assumed in the calculations provide experimentalists with approximate synthesis conditions under which a certain defect landscape is obtained. Defect calculations, on the other hand, could also benefit from additional information from experiments regarding the actual conditions during synthesis, including the possible formation of impurity and/or intermediate phases. It is usually difficult to know the exact experimental conditions to map them onto specific points in the phase diagram at which the formation energies are calculated. Also, a full exploration of high-dimensional chemical-potential phase diagrams, as required for multinary host compounds, may not always be practical. Information about impurity phases or metastable intermediates obtained in, e.g., *in situ* x-ray diffraction [157], therefore, could be useful in helping determine more accurately experimentally relevant areas in the phase diagram. Such joint efforts between theory and experiment would benefit further the understanding and design of complex functional materials.

Acknowledgement

This work made use of computing resources at the Center for Computationally Assisted Science and Technology at North Dakota State University. MDJ acknowledges funding for this project by the Office of Naval Research (ONR) through the Naval Research Laboratorys Basic Research Program.

References

- [1] M. S. Whittingham. Lithium Batteries and Cathode Materials. *Chem. Rev.*, 104(10):4271–4302, 2004.
- [2] B. L. Ellis, K. T. Lee, and L. F. Nazar. Positive Electrode Materials for Li-Ion and Li-Batteries. *Chem. Mater.*, 22(3):691–714, 2010.
- [3] C. Masquelier and L. Croguennec. Polyanionic (Phosphates, Silicates, Sulfates) Frameworks as Electrode Materials for Rechargeable Li (or Na) Batteries. *Chem. Rev.*, 113(8):6552–6591, 2013.
- [4] V. Palomares, M. Casas-Cabanas, E. Castillo-Martinez, M. H. Han, and T. Rojo. Update on Na-based battery materials. A growing research path. *Energy Environ. Sci.*, 6:2312–2337, 2013.
- [5] W. Zuo, R. Li, C. Zhou, Y. Li, J. Xia, and J. Liu. Battery-Supercapacitor Hybrid Devices: Recent Progress and Future Prospects. *Adv. Sci.*, 4(7):1600539, 2017.
- [6] O. Crosnier, N. Goubard-Bretesché, G. Buvat, L. Athouël, C. Douard, P. Lannelongue, F. Favier, and T. Brousse. Polycationic oxides as potential electrode materials for aqueous-based electrochemical capacitor. *Curr. Opin. Electrochem.*, 2018. in press; doi:10.1016/j.coelec.2018.05.005.
- [7] M. M. Kuklja, E. A. Kotomin, R. Merkle, Yu. A. Mastrikov, and J. Maier. Combined theoretical and experimental analysis of processes determining cathode performance in solid oxide fuel cells. *Phys. Chem. Chem. Phys.*, 15:5443–5471, 2013.
- [8] J. A. Kilner and M. Burriel. Materials for Intermediate-Temperature Solid-Oxide Fuel Cells. *Ann. Rev. Mater. Res.*, 44(1):365–393, 2014.
- [9] Z. Gao, L. V. Mogni, E. C. Miller, J. G. Railsback, and S. A. Barnett. A perspective on low-temperature solid oxide fuel cells. *Energy Environ. Sci.*, 9:1602–1644, 2016.
- [10] C. N. R. Rao. Transition Metal Oxides. *Ann. Rev. Phys. Chem.*, 40(1):291–326, 1989.
- [11] K. M. Rabe. First-Principles Calculations of Complex Metal-Oxide Materials. *Ann. Rev. Condens. Matter Phys.*, 1(1):211–235, 2010.
- [12] J. Schoonman, H. L. Tuller, and E. M. Kelder. Defect chemical aspects of lithium-ion battery cathodes. *J. Power Sources*, 81–82:44–48, 1999.
- [13] B. Ellis, L. K. Perry, D. H. Ryan, and L. F. Nazar. Small Polaron Hopping in Li_xFePO_4 Solid Solutions: Coupled Lithium-Ion and Electron Mobility. *J. Am. Chem. Soc.*, 128(35):11416–11422, 2006.
- [14] T. Maxisch, F. Zhou, and G. Ceder. Ab initio study of the migration of small polarons in olivine Li_xFePO_4 and their association with lithium ions and vacancies. *Phys. Rev. B*, 73(10):104301, 2006.
- [15] J. Maier and R. Amin. Defect chemistry of LiFePO_4 . *J. Electrochem. Soc.*, 155(4):A339–A344, 2008.
- [16] P. Axmann, C. Stinner, M. Wohlfahrt-Mehrens, A. Mauger, F. Gendron, and C. M. Julien. Nonstoichiometric LiFePO_4 : Defects and Related Properties. *Chem. Mater.*, 21(8):1636–1644, 2009.
- [17] K. Hoang and M. Johannes. Tailoring Native Defects in LiFePO_4 : Insights from First-Principles Calculations. *Chem. Mater.*, 23(11):3003–3013, 2011.
- [18] P. Hohenberg and W. Kohn. Inhomogeneous Electron Gas. *Phys. Rev.*, 136:B864–B871, 1964.

- [19] W. Kohn and L. J. Sham. Self-Consistent Equations Including Exchange and Correlation Effects. *Phys. Rev.*, 140:A1133–A1138, 1965.
- [20] Y. S. Meng and M. E. Arroyo-de Dompablo. First principles computational materials design for energy storage materials in lithium ion batteries. *Energy Environ. Sci.*, 2:589–609, 2009.
- [21] M. S. Islam and C. A. J. Fisher. Lithium and sodium battery cathode materials: computational insights into voltage, diffusion and nanostructural properties. *Chem. Soc. Rev.*, 43:185–204, 2014.
- [22] A. Urban, D.-H. Seo, and G. Ceder. Computational understanding of Li-ion batteries. *npj Comput. Mater.*, 2:16002, 2016.
- [23] A. Van der Ven and G. Ceder. Lithium diffusion mechanisms in layered intercalation compounds. *J. Power Sources*, 97–98:529–531, 2001.
- [24] D. Morgan, A. Van der Ven, and G. Ceder. Li Conductivity in Li_xMPO_4 ($M = \text{Mn, Fe, Co, Ni}$) Olivine Materials. *Electrochem. Solid-State Lett.*, 7(2):A30–A32, 2004.
- [25] K. Kang and G. Ceder. Factors that affect Li mobility in layered lithium transition metal oxides. *Phys. Rev. B*, 74:094105, 2006.
- [26] S. P. Ong, V. L. Chevrier, and G. Ceder. Comparison of small polaron migration and phase separation in olivine LiMnPO_4 and LiFePO_4 using hybrid density functional theory. *Phys. Rev. B*, 83:075112, 2011.
- [27] M. D. Johannes, K. Hoang, J. L. Allen, and K. Gaskell. Hole polaron formation and migration in olivine phosphate materials. *Phys. Rev. B*, 85:115106, 2012.
- [28] R. Malik, D. Burch, M. Bazant, and G. Ceder. Particle Size Dependence of the Ionic Diffusivity. *Nano Letters*, 10(10):4123–4127, 2010.
- [29] M. S. Islam, D. J. Driscoll, C. A. J. Fisher, and P. R. Slater. Atomic-scale investigation of defects, dopants, and lithium transport in the LiFePO_4 olivine-type battery material. *Chem. Mater.*, 17(20):5085–5092, 2005.
- [30] C. A. J. Fisher, V. M. Hart Prieto, and M. S. Islam. Lithium battery materials LiMPO_4 ($M = \text{Mn, Fe, Co, and Ni}$): Insights into defect association, transport mechanisms, and doping behavior. *Chem. Mater.*, 20(18):5907–5915, 2008.
- [31] G. R. Gardiner and M. S. Islam. Anti-Site Defects and Ion Migration in the $\text{LiFe}_{0.5}\text{Mn}_{0.5}\text{PO}_4$ Mixed-Metal Cathode Material. *Chem. Mater.*, 22(3):1242–1248, 2010.
- [32] F. A. Kröger. *The Chemistry of Imperfect Crystals*. North Holland Publishing Co., Amsterdam, 1974.
- [33] K. Hoang and M. D. Johannes. First-principles studies of the effects of impurities on the ionic and electronic conduction in LiFePO_4 . *J. Power Sources*, 206:274–281, 2012.
- [34] Y. Koyama, H. Arai, I. Tanaka, Y. Uchimoto, and Z. Ogumi. Defect Chemistry in Layered LiMO_2 ($M = \text{Co, Ni, Mn, and Li}_{1/3}\text{Mn}_{2/3}$) by First-Principles Calculations. *Chem. Mater.*, 24(20):3886–3894, 2012.
- [35] Y. Koyama, H. Arai, I. Tanaka, Y. Uchimoto, and Z. Ogumi. High temperature defect chemistry in layered lithium transition-metal oxides based on first-principles calculations. *J. Power Sources*, 244:592–596, 2013.
- [36] K. Hoang and M. D. Johannes. Defect chemistry in layered transition-metal oxides from screened hybrid density functional calculations. *J. Mater. Chem. A*, 2:5224–5235, 2014.
- [37] Y. Koyama, H. Arai, I. Tanaka, Y. Uchimoto, and Z. Ogumi. First principles study of dopant solubility and defect chemistry in LiCoO_2 . *J. Mater. Chem. A*, 2:11235–11245, 2014.
- [38] M. S. Park. First-principles study of native point defects in $\text{LiNi}_{1/3}\text{Co}_{1/3}\text{Mn}_{1/3}\text{O}_2$ and Li_2MnO_3 . *Phys. Chem. Chem. Phys.*, 16:16798–16804, 2014.
- [39] J. A. Santana, J. Kim, P. R. C. Kent, and F. A. Reboredo. Successes and failures of Hubbard-corrected density functional theory: The case of Mg doped LiCoO_2 . *J. Chem. Phys.*, 141(16):164706, 2014.
- [40] K. Hoang. Understanding the electronic and ionic conduction and lithium over-stoichiometry in LiMn_2O_4 spinel. *J. Mater. Chem. A*, 2:18271–18280, 2014.

- [41] K. Hoang. Defect Physics, Delithiation Mechanism, and Electronic and Ionic Conduction in Layered Lithium Manganese Oxide Cathode Materials. *Phys. Rev. Applied*, 3:024013, 2015.
- [42] F. Kong, R. C. Longo, D.-H. Yeon, J. Yoon, J.-H. Park, C. Liang, S. KC, Y. Zheng, S.-G. Doo, and K. Cho. Multivalent Li-Site Doping of Mn Oxides for Li-Ion Batteries. *J. Phys. Chem. C*, 119(38):21904–21912, 2015.
- [43] F. Kong, R. C. Longo, M.-S. Park, J. Yoon, D.-H. Yeon, J.-H. Park, W.-H. Wang, S. KC, S.-G. Doo, and K. Cho. *Ab initio* study of doping effects on LiMnO_2 and Li_2MnO_3 cathode materials for Li-ion batteries. *J. Mater. Chem. A*, 3:8489–8500, 2015.
- [44] K. Hoang and M. Johannes. Defect Physics and Chemistry in Layered Mixed Transition Metal Oxide Cathode Materials: (Ni,Co,Mn) vs (Ni,Co,Al). *Chem. Mater.*, 28(5):1325–1334, 2016.
- [45] K. Hoang. First-principles theory of doping in layered oxide electrode materials. *Phys. Rev. Materials*, 1:075403, 2017.
- [46] K. Hoang. Doping in Li-rich cathode material Li_2MnO_3 : Interplay between lattice site preference, electronic structure, and delithiation mechanism. *Phys. Rev. Materials*, 1:075404, 2017.
- [47] H. Duan, J. Li, H. Du, S. W. Chiang, C. Xu, W. Duan, and F. Kang. Tailoring Native Defects and Zinc Impurities in $\text{Li}_4\text{Ti}_5\text{O}_{12}$: Insights from First-Principles Study. *J. Phys. Chem. C*, 119(9):5238–5245, 2015.
- [48] H. Duan, J. Li, S. W. Chiang, H. Du, and W. Duan. First-principles study of native defects in LiTi_2O_4 . *Comput. Mater. Sci.*, 96:263–267, 2015.
- [49] H. Cho, H. Son, D. Kim, M. Lee, S. Boateng, H. Han, K. M. Kim, S. Kim, H. Choi, T. Song, and K. H. Lee. Impact of Mg-Doping Site Control in the Performance of $\text{Li}_4\text{Ti}_5\text{O}_{12}$ Li-Ion Battery Anode: First-Principles Predictions and Experimental Verifications. *J. Phys. Chem. C*, 121(28):14994–15001, 2017.
- [50] M. D. Radin and D. J. Siegel. Charge transport in lithium peroxide: relevance for rechargeable metal-air batteries. *Energy Environ. Sci.*, 6:2370–2379, 2013.
- [51] J. B. Varley, V. Viswanathan, J. K. Nørskov, and A. C. Luntz. Lithium and oxygen vacancies and their role in Li_2O_2 charge transport in Li- O_2 batteries. *Energy Environ. Sci.*, 7:720–727, 2014.
- [52] M. D. Radin, C. W. Monroe, and D. J. Siegel. How Dopants Can Enhance Charge Transport in Li_2O_2 . *Chem. Mater.*, 27(3):839–847, 2015.
- [53] B. J. Alder D. M. Ceperley. Ground State of the Electron Gas by a Stochastic Method. *Phys. Rev. Lett.*, 45(7):566, 1980.
- [54] J. P. Perdew, J. A. Chevary, S. H. Vosko, K. A. Jackson, M. R. Pederson, D. J. Singh, and C. Fiolhais. Atoms, molecules, solids, and surfaces: Applications of the generalized gradient approximation for exchange and correlation. *Phys. Rev. B*, 46:6671–6687, 1992.
- [55] V. I. Anisimov, J. Zaanen, and O. K. Andersen. Hubbard-corrected density-functional theory. *Phys. Rev. B*, 44(3):943–954, 1991.
- [56] J. P. Perdew, M. Ernzerhof, and K. Burke. Rationale for mixing exact exchange with density functional approximations. *J. Chem. Phys.*, 105(22):9982–9985, 1996.
- [57] C. Franchini. Hybrid functionals applied to perovskites. *J. Phys.: Condens. Matter*, 26(25):253202, 2014.
- [58] J. Heyd, G. E. Scuseria, and M. Ernzerhof. Hybrid functionals based on a screened Coulomb potential. *J. Chem. Phys.*, 118(18):8207–8215, 2003.
- [59] G. Kresse and J. Furthmüller. Efficient iterative schemes for *ab initio* total-energy calculations using a plane-wave basis set. *Phys. Rev. B*, 54(16):11169–11186, 1996.
- [60] S. B. Zhang and J. E. Northrup. Chemical potential dependence of defect formation energies in GaAs: Application to Ga self-diffusion. *Phys. Rev. Lett.*, 67:2339–2342, 1991.
- [61] C. G. Van de Walle, D. B. Laks, G. F. Neumark, and S. T. Pantelides. First-principles calculations of solubilities and doping limits: Li, Na, and N in ZnSe. *Phys. Rev. B*, 47:9425–9434, 1993.
- [62] C. G. Van de Walle and J. Neugebauer. First-principles calculations for defects and impurities: Applications to III-nitrides. *J. Appl. Phys.*, 95(8):3851–3879, 2004.

- [63] C. Freysoldt, B. Grabowski, T. Hickel, J. Neugebauer, G. Kresse, A. Janotti, and C. G. Van de Walle. First-principles calculations for point defects in solids. *Rev. Mod. Phys.*, 86:253–305, 2014.
- [64] J.-M. Doux, K. Hoang, O. Joubert, J. Hamon, F. Massuyeau, and E. Quarez. Ionic to Electronic Transport in $\text{Ba}_3\text{Ti}_3\text{O}_6(\text{BO}_3)_2$ under Reducing Atmosphere. *ACS Appl. Energy Mater.*, 1(2):510–521, 2018.
- [65] C. Freysoldt, J. Neugebauer, and C. G. Van de Walle. Fully *Ab Initio* Finite-Size Corrections for Charged-Defect Supercell Calculations. *Phys. Rev. Lett.*, 102:016402, 2009.
- [66] K. Reuter and M. Scheffler. Composition, structure, and stability of $\text{RuO}_2(110)$ as a function of oxygen pressure. *Phys. Rev. B*, 65:035406, 2001.
- [67] R. J. Gummow, M. M. Thackeray, W. I. F. David, and S. Hull. Structure and electrochemistry of lithium cobalt oxide synthesised at 400°C. *Mater. Res. Bull.*, 27(3):327–337, 1992.
- [68] D. R. Stull and H. Prophet. *JANAF Thermochemical Tables*. U.S. National Bureau of Standards, Washington, D.C., 2nd edition, 1971.
- [69] G. Henkelman, B. P. Uberuaga, and H. Jónsson. A climbing image nudged elastic band method for finding saddle points and minimum energy paths. *J. Chem. Phys.*, 113(22):9901–9904, 2000.
- [70] K. Momma and F. Izumi. *VESTA 3* for three-dimensional visualization of crystal, volumetric and morphology data. *J. Appl. Cryst.*, 44(6):1272–1276, 2011.
- [71] A. Yamada and M. Tanaka. Jahn-Teller structural phase transition around 280 K in LiMn_2O_4 . *Mater. Res. Bull.*, 30(6):715–721, 1995.
- [72] J. Rodríguez-Carvajal, G. Rousse, C. Masquelier, and M. Hervieu. Electronic Crystallization in a Lithium Battery Material: Columnar Ordering of Electrons and Holes in the Spinel LiMn_2O_4 . *Phys. Rev. Lett.*, 81:4660–4663, 1998.
- [73] K. Oikawa, T. Kamiyama, F. Izumi, B. C. Chakoumakos, H. Ikuta, M. Wakihara, J. Li, and Y. Matsui. Structural phase transition of the spinel-type oxide LiMn_2O_4 . *Solid State Ionics*, 109(1–2):35–41, 1998.
- [74] A. S. Wills, N. P. Raju, and J. E. Greedan. Low-Temperature Structure and Magnetic Properties of the Spinel LiMn_2O_4 : A Frustrated Antiferromagnet and Cathode Material. *Chem. Mater.*, 11(6):1510–1518, 1999.
- [75] M. D. Johannes, C. T. Love, and K. Swider-Lyons. Calculations in Li-Ion Battery Materials. In C. Breitkopf and K. Swider-Lyons, editors, *Handbook of Electrochemical Energy*, pages 313–327. Springer-Verlag, Berlin, Germany, 2017.
- [76] M. D. Johannes, K. Swider-Lyons, and C. T. Love. Oxygen character in the density of states as an indicator of the stability of Li-ion battery cathode materials. *Solid State Ionics*, 286:83–89, 2016.
- [77] A. L. Shluger and A. M. Stoneham. Small polarons in real crystals: concepts and problems. *J. Phys.: Condens. Matter*, 5(19):3049–3086, 1993.
- [78] K. Luo, M. R. Roberts, N. Guerrini, N. Tapia-Ruiz, R. Hao, F. Massel, D. M. Pickup, S. Ramos, Y.-S. Liu, J. Guo, A. V. Chadwick, L. C. Duda, and P. G. Bruce. Anion Redox Chemistry in the Cobalt Free 3d Transition Metal Oxide Intercalation Electrode $\text{Li}[\text{Li}_{0.2}\text{Ni}_{0.2}\text{Mn}_{0.6}]\text{O}_2$. *J. Am. Chem. Soc.*, 138(35):11211–11218, 2016.
- [79] K. Luo, M. R. Roberts, R. Hao, N. Guerrini, D. M. Pickup, Y.-S. Liu, K. Edstrom, J. Guo, A. V. Chadwick, L. C. Duda, and P. G. Bruce. Charge-compensation in 3d-transition-metal-oxide intercalation cathodes through the generation of localized electron holes on oxygen. *Nature Chem.*, 8:684–691, 2016.
- [80] O. F. Schirmer. O^- bound small polarons in oxide materials. *J. Phys.: Condens. Matter*, 18(43):R667–R704, 2006.
- [81] K. Hoang. Polaron formation, native defects, and electronic conduction in metal tungstates. *Phys. Rev. Materials*, 1:024603, 2017.
- [82] K. Hoang, M. Oh, and Y. Choi. Electronic structure, polaron formation, and functional properties

- in transition-metal tungstates. *RSC Adv.*, 8:4191–4196, 2018.
- [83] N. A. Chernova, G. M. Nolis, F. O. Omenya, H. Zhou, Z. Li, and M. S. Whittingham. What can we learn about battery materials from their magnetic properties? *J. Mater. Chem.*, 21:9865–9875, 2011.
- [84] M. Ménétrier, D. Carlier, M. Blangero, and C. Delmas. On “Really” Stoichiometric LiCoO₂. *Electrochem. Solid-State Lett.*, 11(11):A179–A182, 2008.
- [85] G. Dutta, A. Manthiram, J. B. Goodenough, and J.-C. Grenier. Chemical synthesis and properties of Li_{1- δ - x} Ni_{1+ δ} O₂ and Li[Ni₂]O₄. *J. Solid State Chem.*, 96(1):123–131, 1992.
- [86] R. Kanno, H. Kubo, Y. Kawamoto, T. Kamiyama, F. Izumi, Y. Takeda, and M. Takano. Phase relationship and lithium deintercalation in lithium nickel oxides. *J. Solid State Chem.*, 110(2):216–225, 1994.
- [87] A. Hirano, R. Kanno, Y. Kawamoto, Y. Takeda, K. Yamaura, M. Takano, K. Ohyama, M. Ohashi, and Y. Yamaguchi. Relationship between non-stoichiometry and physical properties in LiNiO₂. *Solid State Ionics*, 78(1–2):123–131, 1995.
- [88] A.-L. Barra, G. Chouteau, A. Stepanov, A. Rougier, and C. Delmas. High magnetic field properties and ESR of the Li_{1- z} Ni_{1+ z} O₂ compounds. *Eur. Phys. J. B*, 7(4):551–562, 1999.
- [89] E. Chappel, M. D. Núñez Regueiro, S. de Brion, G. Chouteau, V. Bianchi, D. Caurant, and N. Baffier. Interlayer magnetic frustration in quasistoichiometric Li_{1- x} Ni_{1+ x} O₂. *Phys. Rev. B*, 66:132412, 2002.
- [90] P. Kalyani and N. Kalaiselvi. Various aspects of LiNiO₂ chemistry: A review. *Sci. Tech. Adv. Mater.*, 6(6):689–703, 2005.
- [91] A. R. Armstrong and P. G. Bruce. Synthesis of layered LiMnO₂ as an electrode for rechargeable lithium batteries. *Nature*, 381:499–500, 1996.
- [92] F. Capitaine, P. Gravereau, and C. Delmas. A new variety of LiMnO₂ with a layered structure. *Solid State Ionics*, 89(3–4):197–202, 1996.
- [93] G. Vitins and K. West. Lithium Intercalation into Layered LiMnO₂. *J. Electrochem. Soc.*, 144(8):2587–2592, 1997.
- [94] K. Kubota, T. Kaneko, M. Hirayama, M. Yonemura, Y. Imanari, K. Nakane, and R. Kanno. Direct synthesis of oxygen-deficient Li₂MnO_{3- x} for high capacity lithium battery electrodes. *J. Power Sources*, 216:249–255, 2012.
- [95] S. Levasseur, M. Ménétrier, Y. Shao-Horn, L. Gautier, A. Audemer, G. Demazeau, A. Largeau, and C. Delmas. Oxygen Vacancies and Intermediate Spin Trivalent Cobalt Ions in Lithium-Overstoichiometric LiCoO₂. *Chem. Mater.*, 15(1):348–354, 2003.
- [96] K. Hoang, A. Janotti, and C. G. Van de Walle. Mechanisms for the decomposition and dehydrogenation of Li amide/imide. *Phys. Rev. B*, 85:064115, 2012.
- [97] C. S. Yoon, M.-J. Choi, D.-W. Jun, Q. Zhang, P. Kaghazchi, K.-H. Kim, and Y.-K. Sun. Cation Ordering of Zr-Doped LiNiO₂ Cathode for Lithium-Ion Batteries. *Chem. Mater.*, 30(5):1808–1814, 2018.
- [98] J. Xiao, N. A. Chernova, and M. S. Whittingham. Layered mixed transition metal oxide cathodes with reduced cobalt content for lithium ion batteries. *Chem. Mater.*, 20(24):7454–7464, 2008.
- [99] J. Liang, D. Wu, M. Hu, Y. Tian, J. Wei, and Z. Zhou. Could Li/Ni Disorder be Utilized Positively? Combined Experimental and Computational Investigation on Pillar Effect of Ni at Li Sites on LiCoO₂ at High Voltages. *Electrochim. Acta*, 146:784–791, 2014.
- [100] S. F. Yang, Y. N. Song, P. Y. Zavalij, and M. S. Whittingham. Reactivity, stability and electrochemical behavior of lithium iron phosphates. *Electrochem. Commun.*, 4(3):239–244, 2002.
- [101] J. J. Chen, M. J. Vacchio, S. J. Wang, N. Chernova, P. Y. Zavalij, and M. S. Whittingham. The hydrothermal synthesis and characterization of olivines and related compounds for electrochemical applications. *Solid State Ionics*, 178(31–32):1676–1693, 2008.
- [102] S.-Y. Chung, S.-Y. Choi, T. Yamamoto, and Y. Ikuhara. Atomic-Scale Visualization of Antisite Defects in LiFePO₄. *Phys. Rev. Lett.*, 100(12):125502, 2008.

- [103] K.-Y. Park, I. Park, H. Kim, G. Yoon, H. Gwon, Y. Cho, Y. S. Yun, J.-J. Kim, S. Lee, D. Ahn, Y. Kim, H. Kim, I. Hwang, W.-S. Yoon, and K. Kang. Lithium-excess olivine electrode for lithium rechargeable batteries. *Energy Environ. Sci.*, 9:2902–2915, 2016.
- [104] J. L. Allen, T. R. Jow, and J. Wolfenstine. Improved cycle life of Fe-substituted LiCoPO_4 . *J. Power Sources*, 196(20):8656–8661, 2011.
- [105] Q. D. Truong, M. K. Devaraju, T. Tomai, and I. Honma. Direct Observation of Antisite Defects in LiCoPO_4 Cathode Materials by Annular Dark- and Bright-Field Electron Microscopy. *ACS Appl. Mater. Interfaces*, 5(20):9926–9932, 2013.
- [106] A. Boulineau and T. Gutel. Revealing Electrochemically Induced Antisite Defects in LiCoPO_4 : Evolution upon Cycling. *Chem. Mater.*, 27(3):802–807, 2015.
- [107] M. K. Devaraju, Q. D. Truong, H. Hyodo, Y. Sasaki, and I. Honma. Synthesis, characterization and observation of antisite defects in LiNiPO_4 nanomaterials. *Sci. Rep.*, 5:11041, 2015.
- [108] J. Jacas Biendicho, K.-C. Hsiao, S. Hull, and A. R. West. Investigation of Antisite Defect Formation and Chemical Expansion in LiNiPO_4 by in Situ Neutron Diffraction. *Inorg. Chem.*, 56(6):3657–3662, 2017.
- [109] S. P. Ong, L. Wang, B. Kang, and G. Ceder. Li–Fe–P–O₂ Phase Diagram from First Principles Calculations. *Chem. Mater.*, 20(5):1798–1807, 2008.
- [110] J. M. Tarascon, W. R. McKinnon, F. Coowar, T. N. Bowmer, G. Amatucci, and D. Guyomard. Synthesis Conditions and Oxygen Stoichiometry Effects on Li Insertion into the Spinel LiMn_2O_4 . *J. Electrochem. Soc.*, 141(6):1421–1431, 1994.
- [111] Y. Xia and M. Yoshio. An Investigation of Lithium Ion Insertion into Spinel Structure LiMn_2O_4 Compounds. *J. Electrochem. Soc.*, 143(3):825–833, 1996.
- [112] J. M. Paulsen and J. R. Dahn. Phase Diagram of Li–Mn–O Spinel in Air. *Chem. Mater.*, 11(11):3065–3079, 1999.
- [113] Y. J. Lee and C. P. Grey. ^6Li Magic Angle Spinning Nuclear Magnetic Resonance Study of the Cathode Materials $\text{Li}_{1+\alpha}\text{Mn}_{2-\alpha}\text{O}_{4-\delta}$: The Effect of Local Structure on the Electrochemical Properties. *J. Electrochem. Soc.*, 149(2):A103–A114, 2002.
- [114] S. Martinez, I. Sobrados, D. Tonti, J. M. Amarilla, and J. Sanz. Chemical vs. electrochemical extraction of lithium from the Li-excess $\text{Li}_{1.10}\text{Mn}_{1.90}\text{O}_4$ spinel followed by NMR and DRX techniques. *Phys. Chem. Chem. Phys.*, 16:3282–3291, 2014.
- [115] J. Sugiyama, K. Mukai, Y. Ikeda, P. L. Russo, T. Suzuki, I. Watanabe, J. H. Brewer, E. J. Ansaldi, K. H. Chow, K. Ariyoshi, and T. Ohzuku. Microscopic magnetic and structural nature of spinel $\text{Li}[\text{Li}_x\text{Mn}_{2-x}]\text{O}_4$. *Phys. Rev. B*, 75:174424, 2007.
- [116] K. Kamazawa, H. Nozaki, M. Harada, K. Mukai, Y. Ikeda, K. Iida, T. J. Sato, Y. Qiu, M. Tyagi, and J. Sugiyama. Interrelationship between Li^+ diffusion, charge, and magnetism in $^7\text{LiMn}_2\text{O}_4$ and $^7\text{Li}_{1.1}\text{Mn}_{1.9}\text{O}_4$ spinels: Elastic, inelastic, and quasielastic neutron scattering. *Phys. Rev. B*, 83:094401, 2011.
- [117] R. J. Gummow, A. de Kock, and M. M. Thackeray. Improved capacity retention in rechargeable 4 V lithium/lithium-manganese oxide (spinel) cells. *Solid State Ionics*, 69(1):59–67, 1994.
- [118] R. J. Cava, D. W. Murphy, S. Zahurak, A. Santoro, and R. S. Roth. The crystal structures of the lithium-inserted metal oxides $\text{Li}_{0.5}\text{TiO}_2$ anatase, LiTi_2O_4 spinel, and $\text{Li}_2\text{Ti}_2\text{O}_4$. *J. Solid State Chem.*, 53(1):64–75, 1984.
- [119] K. M. Colbow, J. R. Dahn, and R. R. Haering. Structure and electrochemistry of the spinel oxides LiTi_2O_4 and $\text{Li}_{4/3}\text{Ti}_{5/3}\text{O}_4$. *J. Power Sources*, 26(3):397–402, 1989.
- [120] E. G. Moshopoulou. Superconductivity in the Spinel Compound LiTi_2O_4 . *J. Am. Ceram. Soc.*, 82(12):3317–3320, 1999.
- [121] P. Kalyani, S. Chitra, T. Mohan, and S. Gopukumar. Lithium metal rechargeable cells using Li_2MnO_3 as the positive electrode. *J. Power Sources*, 80(1–2):103–106, 1999.
- [122] M. Sathiya, K. Ramesha, G. Rousse, D. Foix, D. Gonbeau, A. S. Prakash, M. L. Doublet, K. Hemalatha, and J.-M. Tarascon. High Performance $\text{Li}_2\text{Ru}_{1-y}\text{Mn}_y\text{O}_3$ ($0.2 \leq y \leq 0.8$) Cathode Materials for Rechargeable Lithium-Ion Batteries: Their Understanding. *Chem.*

- Mater.*, 25(7):1121–1131, 2013.
- [123] W. Yao, M.-T. Sougrati, K. Hoang, J. Hui, P. Lightfoot, and A. R. Armstrong. $\text{Na}_2\text{Fe}(\text{C}_2\text{O}_4)\text{F}_2$: A New Iron-Based Polyoxyanion Cathode for Li/Na Ion Batteries. *Chem. Mater.*, 29(5):2167–2172, 2017.
 - [124] W. Yao, M.-T. Sougrati, K. Hoang, J. Hui, P. Lightfoot, and A. R. Armstrong. Reinvestigation of $\text{Na}_2\text{Fe}_2(\text{C}_2\text{O}_4)_3 \cdot 2\text{H}_2\text{O}$: An Iron-Based Positive Electrode for Secondary Batteries. *Chem. Mater.*, 29(21):9095–9101, 2017.
 - [125] M. K. Aydinol, A. F. Kohan, G. Ceder, K. Cho, and J. Joannopoulos. Ab initio study of lithium intercalation in metal oxides and metal dichalcogenides. *Phys. Rev. B*, 56:1354–1365, 1997.
 - [126] K. M. Rosso, D. M. A. Smith, and M. Dupuis. An ab initio model of electron transport in hematite ($\alpha\text{-Fe}_2\text{O}_3$) basal planes. *J. Chem. Phys.*, 118(14):6455–6466, 2003.
 - [127] N. Iordanova, M. Dupuis, and K. M. Rosso. Charge transport in metal oxides: A theoretical study of hematite $\alpha\text{-Fe}_2\text{O}_3$. *J. Chem. Phys.*, 122(14):144305, 2005.
 - [128] R. J. D. Tilley. *Defects in Solids*. Special Topics in Inorganic Chemistry. Wiley, 2008.
 - [129] M. Ménétrier, I. Saadoune, S. Levasseur, and C. Delmas. The insulator-metal transition upon lithium deintercalation from LiCoO_2 : electronic properties and ^7Li NMR study. *J. Mater. Chem.*, 9:1135–1140, 1999.
 - [130] S. Levasseur, M. Ménétrier, and C. Delmas. On the Dual Effect of Mg Doping in LiCoO_2 and $\text{Li}_{1+\delta}\text{CoO}_2$: Structural, Electronic Properties, and ^7Li MAS NMR Studies. *Chem. Mater.*, 14(8):3584–3590, 2002.
 - [131] F. Nobili, R. Tossici, R. Marassi, F. Croce, and B. Scrosati. An AC Impedance Spectroscopic Study of Li_xCoO_2 at Different Temperatures. *J. Phys. Chem. B*, 106(15):3909–3915, 2002.
 - [132] F. Nobili, S. Dsoke, F. Croce, and R. Marassi. An ac impedance spectroscopic study of Mg-doped LiCoO_2 at different temperatures: electronic and ionic transport properties. *Electrochim. Acta*, 50(11):2307–2313, 2005.
 - [133] Q. Lin, Q. Li, K. E. Gray, and J. F. Mitchell. Vapor Growth and Chemical Delithiation of Stoichiometric LiCoO_2 Crystals. *Cryst. Growth Des.*, 12(3):1232–1238, 2012.
 - [134] S. Wang, M. Yan, Y. Li, C. Vinado, and J. Yang. Separating electronic and ionic conductivity in mix-conducting layered lithium transition-metal oxides. *J. Power Sources*, 393:75–82, 2018.
 - [135] J. Molenda, P. Wilk, and J. Marzec. Structural, electrical and electrochemical properties of LiNiO_2 . *Solid State Ionics*, 146(1–2):73–79, 2002.
 - [136] I. Saadoune and C. Delmas. On the $\text{Li}_x\text{Ni}_{0.8}\text{Co}_{0.2}\text{O}_2$ System. *J. Solid State Chem.*, 136(1):8–15, 1998.
 - [137] R. Amin, D. B. Ravnsbæk, and Y.-M. Chiang. Characterization of Electronic and Ionic Transport in $\text{Li}_{1-x}\text{Ni}_{0.8}\text{Co}_{0.15}\text{Al}_{0.05}\text{O}_2$ (NCA). *J. Electrochem. Soc.*, 162(7):A1163–A1169, 2015.
 - [138] R. Amin and Y.-M. Chiang. Characterization of Electronic and Ionic Transport in $\text{Li}_{1-x}\text{Ni}_{0.33}\text{Mn}_{0.33}\text{Co}_{0.33}\text{O}_2$ (NMC₃₃₃) and $\text{Li}_{1-x}\text{Ni}_{0.50}\text{Mn}_{0.20}\text{Co}_{0.30}\text{O}_2$ (NMC₅₂₃) as a Function of Li Content. *J. Electrochem. Soc.*, 163(8):A1512–A1517, 2016.
 - [139] H.-J. Noh, S. Youn, C. S. Yoon, and Y.-K. Sun. Comparison of the structural and electrochemical properties of layered $\text{Li}[\text{Ni}_x\text{Co}_y\text{Mn}_z]\text{O}_2$ ($x = 1/3, 0.5, 0.6, 0.7, 0.8$ and 0.85) cathode material for lithium-ion batteries. *J. Power Sources*, 233:121–130, 2013.
 - [140] J. Molenda, W. Ojczyk, K. Świerczek, W. Zajac, F. Krok, J. Dygas, and R.-S. Liu. Diffusional mechanism of deintercalation in $\text{LiFe}_{1-y}\text{Mn}_y\text{PO}_4$ cathode material. *Solid State Ionics*, 177(26–32):2617–2624, 2006.
 - [141] K. Zaghib, A. Mauger, J. B. Goodenough, F. Gendron, and C. M. Julien. Electronic, Optical, and Magnetic Properties of LiFePO_4 : Small Magnetic Polaron Effects. *Chem. Mater.*, 19(15):3740–3747, 2007.
 - [142] R. Amin, J. Maier, P. Balaya, D. P. Chen, and C. T. Lin. Ionic and electronic transport in single crystalline LiFePO_4 grown by optical floating zone technique. *Solid State Ionics*, 179(27–32):1683–1687, 2008.
 - [143] V. Massarotti, D. Capsoni, M. Bini, G. Chiodelli, C. B. Azzoni, M. C. Mozzati, and A. Paleari.

- Characterization of Sol-Gel LiMn_2O_4 Spinel Phase. *J. Solid State Chem.*, 147(2):509–515, 1999.
- [144] E. Iguchi, Y. Tokuda, H. Nakatsugawa, and F. Munakata. Electrical transport properties in LiMn_2O_4 , $\text{Li}_{0.95}\text{Mn}_2\text{O}_4$, and $\text{LiMn}_{1.95}\text{B}_{0.05}\text{O}_4$ ($\text{B} = \text{Al}$ or Ga) around room temperature. *J. Appl. Phys.*, 91(4):2149–2154, 2002.
- [145] T.-T. Fang and H.-Y. Chung. Reassessment of the Electronic-Conduction Behavior above the Verwey-Like Transition of Ni^{2+} - and Al^{3+} -Doped LiMn_2O_4 . *J. Am. Ceram. Soc.*, 91(1):342–345, 2008.
- [146] S. Takai, K. Yoshioka, H. Iikura, M. Matsubayashi, T. Yao, and T. Esaka. Tracer diffusion coefficients of lithium ion in LiMn_2O_4 measured by neutron radiography. *Solid State Ionics*, 256:93–96, 2014.
- [147] Z. Lu, D. D. MacNeil, and J. R. Dahn. Layered Cathode Materials $\text{Li}[\text{Ni}_x\text{Li}_{1/3-2x/3}\text{Mn}_{2/3-x/3}]\text{O}_2$ for Lithium-Ion Batteries. *Electrochem. Solid-State Lett.*, 4(11):A191–A194, 2001.
- [148] Z. Lu, L. Y. Beaulieu, R. A. Donabarger, C. L. Thomas, and J. R. Dahn. Synthesis, Structure, and Electrochemical Behavior of $\text{Li}[\text{Ni}_x\text{Li}_{1/3-2x/3}\text{Mn}_{2/3-x/3}]\text{O}_2$. *J. Electrochem. Soc.*, 149(6):A778–A791, 2002.
- [149] A. Peles and C. G. Van de Walle. Role of charged defects and impurities in kinetics of hydrogen storage materials: A first-principles study. *Phys. Rev. B*, 76(21):214101, 2007.
- [150] K. Hoang and C. G. Van de Walle. Hydrogen-related defects and the role of metal additives in the kinetics of complex hydrides: A first-principles study. *Phys. Rev. B*, 80(21):214109, 2009.
- [151] G. B. Wilson-Short, A. Janotti, K. Hoang, A. Peles, and C. G. Van de Walle. First-principles study of the formation and migration of native defects in NaAlH_4 . *Phys. Rev. B*, 80(22):224102, 2009.
- [152] R. Amin, C. Lin, and J. Maier. Aluminium-doped LiFePO_4 single crystals Part I. Growth, characterization and total conductivity. *Phys. Chem. Chem. Phys.*, 10:3519–3523, 2008.
- [153] R. Amin, C. Lin, and J. Maier. Aluminium-doped LiFePO_4 single crystals Part II. Ionic conductivity, diffusivity and defect model. *Phys. Chem. Chem. Phys.*, 10:3524–3529, 2008.
- [154] M. Sathiyar, G. Rousse, K. Ramesha, C. P. Laisa, H. Vezin, M. T. Sougrati, M. L. Doublet, D. Foix, D. Gonbeau, W. Walker, A. S. Prakash, M. B. Hassine, L. Dupont, and J.-M. Tarascon. Reversible anionic redox chemistry in high-capacity layered-oxide electrodes. *Nat. Mater.*, 12:827–835, 2013.
- [155] M. Sathiyar, A. M. Abakumov, D. Foix, G. Rousse, K. Ramesha, M. Saubanère, M. L. Doublet, H. Vezin, C. P. Laisa, A. S. Prakash, D. Gonbeau, G. VanTendeloo, and J.-M. Tarascon. Origin of voltage decay in high-capacity layered oxide electrodes. *Nat. Mater.*, 14:230–238, 2015.
- [156] S. Han, Y. Xia, Z. Wei, B. Qiu, L. Pan, Q. Gu, Z. Liu, and Z. Guo. A comparative study on the oxidation state of lattice oxygen among $\text{Li}_{1.14}\text{Ni}_{0.136}\text{Co}_{0.136}\text{Mn}_{0.544}\text{O}_2$, Li_2MnO_3 , $\text{LiNi}_{0.5}\text{Co}_{0.2}\text{Mn}_{0.3}\text{O}_2$ and LiCoO_2 for the initial charge-discharge. *J. Mater. Chem. A*, 3:11930–11939, 2015.
- [157] D. P. Shoemaker, Y.-J. Hu, D. Y. Chung, G. J. Halder, P. J. Chupas, L. Soderholm, J. F. Mitchell, and M. G. Kanatzidis. In situ studies of a platform for metastable inorganic crystal growth and materials discovery. *Proc. Natl. Acad. Sci. U.S.A.*, 111(30):10922–10927, 2014.